

Breaking-induced energy dissipation of surface gravity waves at varying scales and co-flowing wind stresses

Rui Cao^{1,2,3}, Enrique M. Padilla⁴, Xu Chen^{1,2} and Adrian H. Callaghan^{3,*}

¹State Key Laboratory of Physical Oceanography, Ocean University of China, Qingdao 266100, China

²College of Oceanic and Atmospheric Sciences, Ocean University of China, Qingdao 266100, China

³Department of Civil and Environmental Engineering, Imperial College London, London SW7 2AZ, UK

⁴Barcelona School of Industrial Engineering, Universitat Politècnica de Catalunya (UPC), Barcelona 08034, Spain

*Corresponding author: a.callaghan@imperial.ac.uk

Contributing authors: r.cao@ouc.edu.cn, enrique.padilla@upc.edu, chenxu001@ouc.edu.cn

1 June 2026

Abstract

Breaking-induced energy dissipation is studied for individual unsteady breaking waves using laboratory measurements of unidirectional surface gravity wave groups across a range of underlying wave scales and wind stresses. A refined framework to estimate the breaking-induced energy dissipation ΔE_{br} is first proposed which accounts for background dissipation arising from non-breaking processes. Using this framework, we show that variations in wave scale primarily influence breaking energetics, such as the fractional energy dissipation $\Delta E_{br}/E_0$ and the associated dissipation rate ϵ_b , by modifying the breaking onset threshold. We also show that the presence of co-flowing wind systematically reduces both $\Delta E_{br}/E_0$ and ϵ_b compared to unforced conditions without wind, as wind-forced waves break earlier and have a reduced degree of crest forward-leaning. Exploiting the ability of the crest-front steepness at incipient breaking $\mathcal{S}_{\text{front}}(t_b)$ to characterise both the breaking onset threshold and the local crest geometry, an appropriate scaling for ϵ_b is subsequently formulated based on this local measure. This leads to a relation for fractional energy dissipation of the form $\Delta E_{br}/E_0 \propto \beta^* \mathcal{S}_b (\tau_b/T_b)$, where β^* , \mathcal{S}_b and τ_b/T_b represent the degree of crest forward leaning, the local steepness, and the non-dimensional breaking duration. This scaling explicitly highlights that crest asymmetry and breaking duration play an important role in setting the breaking wave energy dissipation. Finally, we consider the implications for the breaking strength parameter b by first assessing existing steepness-based scaling laws, and subsequently relating b to $\mathcal{S}_{\text{front}}(t_b)$ which yields an approximately linear dependence once the breaking-onset threshold is considered.

1 Introduction

The surface wave energy balance comprises three primary processes: energy input from the wind, non-linear energy re-distribution across different underlying wave components and energy dissipation (Hasselmann, 1961). Among these, energy dissipation is to a large extent controlled by wave breaking, whose underlying physics remains incompletely understood (Drazen et al.,

2008; Herman et al., 2026). Consequently, wave breaking acts as the primary mechanism limiting the growth of surface waves and regulating their evolution under continuous wind forcing (Hasselmann, 1961; Melville, 2003; Perlin et al., 2013; Callaghan, 2018; Hogan et al., 2025). In a broader context, wave breaking plays a direct role in air–sea exchange processes and provides a key physical constraint for spectral wave modelling (Deike, 2022; Callaghan et al., 2025). Accurately characterising both the severity and the rate of energy dissipation associated with individual breaking events therefore remains an active area of research.

1.1 Background

Owing to the considerable technical challenges involved in directly resolving the detailed energetics of individual breaking events in the open ocean, with only very limited observations reported to date (e.g. Callaghan, 2025), much of our present knowledge of breaking-induced energy dissipation (rates) has been derived from controlled laboratory experiments (e.g. Duncan, 1981; Ramberg and Griffin, 1987; Rapp et al., 1990; Kway et al., 1998; Drazen et al., 2008; Tian et al., 2010, 2012; Callaghan et al., 2013, 2016; Deane et al., 2016; Craciunescu and Christou, 2020; Sinnis et al., 2021; Cao et al., 2023, 2026b) and numerical simulations (e.g. Iafrati, 2011; Derakhti and Kirby, 2014, 2016; Deike et al., 2016; De Vita et al., 2018; Mostert et al., 2022; Liu et al., 2023; Scapin et al., 2026). Because in these settings the characteristic length and time scales ($\sim \mathcal{O}(1\text{ m})$ and $\mathcal{O}(1\text{ s})$) of the breakers are typically smaller than those in the open ocean, energy dissipation has commonly been expressed by means of a non-dimensional form, defined as the ratio of the total energy lost during breaking, ΔE_{br} , to the initial energy contained within the wave group, E_0 . Across a wide range of breaking conditions, this fractional energy loss has been reported to lie between $\Delta E_{br}/E_0 \sim \mathcal{O}(1\%)$ and $\mathcal{O}(10\%)$ (Rapp et al., 1990; Kway et al., 1998; Zhang, 2005; Tian et al., 2010; Allis, 2013).

In a similar spirit, energy dissipation rates associated with breaking have often been non-dimensionalised following the framework introduced by Duncan (1981), in which the dissipation rate is characterised by the breaking strength parameter,

$$b = (g\rho_w^{-1})\epsilon_b c^{-5}. \quad (1)$$

Here, g is the gravitational acceleration, ρ_w is the water density, ϵ_b is the rate of energy dissipation per unit crest length (spanwise-averaged) due to wave breaking, and c represents a measure of breaker’s phase speed. Considerable effort has been devoted to constraining b , motivated by the prospect that, once its dependence on wave steepness is established (e.g. Drazen et al., 2008), measurements of c alone may be sufficient to infer the magnitude of ϵ_b using (1) across a range of breaking scales.

Both physical arguments and experimental measurements have consistently shown that wave steepness, \mathcal{S} , is the primary geometric variable controlling variations in the breaking-induced, dimensionless energy dissipation ($\Delta E_{br}/E_0$) as well as the breaking strength parameter (b) (Rapp et al., 1990; Drazen et al., 2008; Romero et al., 2012; Perlin et al., 2013; Deike, 2022). While wave steepness has been defined in different ways across studies, it is generally constructed from a combination of some characteristic wave amplitude, a , and some characteristic wavenumber, k , such that $\mathcal{S} \sim ak$. Notwithstanding differences in the precise definition of wave steepness, there is broad agreement that, for individual breaking events, $\Delta E_{br}/E_0$ increases monotonically with \mathcal{S} at low steepness and may approach an upper bound as breaking becomes sufficiently energetic or involves multiple breaking processes. The breaking strength parameter, b , has likewise been reported to be constrained by a power-law dependence on wave steepness,

$$b \propto \mathcal{S}^{\Xi}, \quad (2)$$

where the exponent $\Xi = 5/2$ is obtained when inertial scaling arguments for turbulent dissipation are adopted (Drazen et al., 2008). This scaling, or variations thereof, have been followed in related studies (Romero et al., 2012; Grare et al., 2013; Deike et al., 2016; De Vita et al., 2018; Craciunescu and Christou, 2020; Simnis et al., 2021; Mostert et al., 2022; Scapin et al., 2026). In these studies, wave steepness was defined explicitly as:

$$\mathcal{S} \sim \mathcal{S}_n = \sum_{i=1}^N a_i k_i, \quad (3)$$

which represents the maximum linear target steepness of a propagating wave group composed of N underlying components. Reported values of Ξ in equation (2) are, however, sensitive to the specific definition of \mathcal{S} employed, with smaller exponents in the range $\Xi \in [1, 2.5]$ obtained in other formulations (Tian et al., 2010; Derakhti and Kirby, 2016; Cao et al., 2023), highlighting the challenge when comparing results from different studies that employ different underlying measures of wave steepness.

1.2 Problem formulation and objectives

Although breaking-induced energy loss and dissipation rates are commonly nondimensionalised, and scaled using wave steepness owing to its close link with wave non-linearity and breaker intensity, available evidence indicates that an intrinsic scale dependence remains.

For example, for a given value of \mathcal{S}_n , breaking waves of different scales have been observed to exhibit systematically different levels of fractional energy dissipation, $\Delta E_{br}/E_0$, as evident in figure 3(a) of Perlin et al. (2013). In addition, laboratory experiments on two-dimensional, unsteady, dispersively focused breaking waves by Drazen et al. (2008) showed that larger-scale breakers, characterised by longer wavelengths (or smaller frequencies), generally dissipate a greater fraction of their energy than smaller-scale breakers, despite being generated at comparable target steepness (see their figure 8). In that study, wave scale was characterised using the central frequency, f_c , of the constant-steepness spectra employed. Evidence of a similar scale dependence has also been reflected in previous b - \mathcal{S}_n relationships. For example, Derakhti and Kirby (2016) numerically reproduced selected breaking wave groups from Drazen et al. (2008) at $f_c = 0.88$ Hz and from Tian et al. (2012) at $f_c = 1.7$ Hz, and showed in their figure 14(b) that values of b associated with larger-scale cases are systematically larger at comparable \mathcal{S}_n those associated with smaller-scale cases. It is important to note that, in the experiments of Drazen et al. (2008) and the corresponding numerical reproductions considered by Derakhti and Kirby (2016), variations in f_c are naturally accompanied by changes in spectral bandwidth, such that the effects of wave scale and bandwidth are not cleanly separated. One aim of the present work is therefore to isolate the role of wave scale and to examine its influence on breaking-induced energy dissipation (and its rates) under more controlled conditions.

In addition to wave scale, previous studies have highlighted the influence of a range of wave and spectral parameters that can modify the relationships between $\Delta E_{br}/E_0$, the breaking strength parameter, b , and \mathcal{S} . These include wave directionality (Wu and Nepf, 2002; Allis, 2013), the mechanism of wave group formation (e.g. dispersive focusing versus modulational instability, Banner and Peirson, 2007; Allis, 2013; Derakhti and Kirby, 2016), spectral bandwidth (Simnis et al., 2021; Cao et al., 2023), water depth (Liu et al., 2023), and the presence of background currents (Wu and Yao, 2004). It remains unclear, however, how direct wind forcing alters these relationships, despite the fact that the majority of breaking events in the ocean occur under wind-forced conditions. To date, only a limited number of studies have explicitly examined the influence of wind on breaking-induced energy dissipation, and the findings reported are mixed. For example, the numerical study of Iafrazi et al. (2019) found no

significant difference in fractional energy dissipation between wind-forced and non-wind-forced cases. Very recently, the DNS results of [Scapin et al. \(2026\)](#) showed that the $b \propto \mathcal{S}_n^{5/2}$ scaling remains valid for wind-forced breakers. In contrast, the combined experimental and numerical results of [Galchenko et al. \(2012\)](#) suggested that direct wind forcing can reduce the energy loss of individual breaking events while increasing the likelihood of breaking.

In our previous work ([Cao et al., 2026a](#)), among others (e.g. [Saket et al., 2017](#); [Knobler et al., 2022](#)), the manner in which direct wind stress modifies the wave shape at incipient breaking has been clarified. Here, we aim to systematically examine how direct wind stress influences breaking-induced energy dissipation, the associated dissipation rate and b , and to interpret these effects in the context of wind-induced modifications to the local crest geometry.

With the above aims in mind, we make use of existing laboratory datasets to address outstanding questions regarding the roles of wave scale and direct (co-flowing) wind stress in controlling the energy dissipation associated with breaking surface gravity waves. Our paper proceeds as follows. Details of the experimental datasets are described in §2. In §3, we introduce a refined framework for quantifying the energy loss due to breaking, ΔE_{br} , in laboratory conditions, alongside a brief reassessment of methods employed in previous studies. The experimental results and their interpretation are presented in §4, followed by a summary of the key findings and implications of the present work in §5.

2 Descriptions of the datasets: *SIREN*, *BUBER* and *EURUS*

The laboratory measurements of surface breaking waves analysed in the present study were obtained from three experimental campaigns, formally referred to as *SIREN*, *BUBER*, and *EURUS*. All three campaigns were conducted in the Hydrodynamics Laboratory of the Department of Civil and Environmental Engineering at Imperial College London. These datasets have contributed to a number of recent studies addressing different aspects of wave mechanics (e.g. [Padilla et al., 2023](#); [Cao et al., 2025](#); [Xu et al., 2025](#); [Cao et al., 2026b](#)). A detailed description of the experimental facilities, wave generation procedures, wave conditions, and measurement systems can be found in §2 of [Cao et al. \(2026a\)](#). Here, we provide only a brief overview of the measurements and wave group configurations directly relevant to the present work and refer the reader to that study for further details.

2.1 Generation of wave groups

Experiments in all three campaigns were carried out in a glass-walled, wind-wave flume with dimensions of 27 m in length, 0.30 m in width, and a constant water depth of $d = 0.70$ m, equipped with flap-type paddles at either end of the flume. Individual breaking waves were generated within dispersively-focused, unsteady wave groups following the technique of [Rapp et al. \(1990\)](#). This technique allows energetic or breaking events to be produced at a prescribed location and time by appropriately tuning the phases of the constituent Fourier components. In our experiments, breaking was targeted at a streamwise location of approximately $x \approx 9.5$ m from the wavemaker.

Wave groups were generated using JONSWAP-type NewWave variance-density spectra, and their properties were characterised by three spectral parameters: (i) the linear amplitude sum of all Fourier components, $A = \sum_{i=1}^N a_i$, which controls the degree of wave-group nonlinearity; (ii) the peak enhancement factor, γ , which determines the concentration of spectral energy around the peak frequency f_p and thus controls the spectral bandwidth; and (iii) the peak wave period, $T_p = 1/f_p = 2\pi/\omega_p$; values of T_p were varied to modify the characteristic wave scale, with larger values of T_p corresponding to larger-scale waves.

We use JONSWAP-type spectra because they are more representative of realistic ocean wave conditions (McAllister et al., 2024), while allowing the wave scale to be adjusted through T_p with a prescribed spectral bandwidth set by γ and an approximately self-similar spectral shape (Cao et al., 2026a).

2.2 Wave group details

Consistent with the objectives outlined in §1.2, the *SIREN* campaign was designed to investigate the role of wave scale, whereas the *BUBER* and *EURUS* campaigns were used to examine the effects of direct wind forcing. The specific wave-group parameters employed in each campaign, including A , γ , and T_p , are summarised in table 1 of Cao et al. (2026a). Briefly, wave groups in all three campaigns had a fixed repeat period of 64 s, resulting in a uniform frequency resolution of $\delta f = 1/64$ Hz. The discrete frequency components spanned the range from a fixed lower bound of $f = 0.406$ Hz to an upper bound of $f = 3f_p$, giving a total number of spectral components $N = 1 + (3f_p - 0.406)/\delta f$.

In the *SIREN* campaign, we varied the peak wave period over the range $T_p \in [1.0, 1.6]$ s in increments of 0.1 s for cases with $\gamma = 2$, in order to cover a broad range of wave scales while keeping the spectral shape self-similar. Additional cases with $T_p = [1.1, 1.3, 1.5]$ s were considered for $\gamma = 3$. The spectral bandwidth, quantified using the parameter $\varepsilon_1 = \sqrt{(m_1 m_{-1}) m_0^{-2}} - 1$ (Saulnier et al., 2011), was calculated to be $\varepsilon_1 = 0.271$ for $\gamma = 2$ and $\varepsilon_1 = 0.254$ for $\gamma = 3$. Here, m_n denotes the n th-order spectral moment of the surface elevation variance-density spectrum, $S_{\eta\eta}(f_i) = a_i^2/(2\delta f)$. For each set of (T_p, γ) , the linear amplitude sum A was progressively increased from $A = 20$ mm up to the largest value for which isolated breaking events could be produced (i.e. we did not consider multiple breaking waves within a single wave group), thereby covering a range of non-breaking and breaking wave groups.

For the other two campaigns (*BUBER* and *EURUS*), wave groups were generated with $T_p = 1.2$ and 1.3 s, and $\gamma = 2$ and 3, and were conducted either without wind or under continuous co-flowing wind forcing at different wind speed levels. The *BUBER* dataset corresponds to the no-wind reference cases, whereas the *EURUS* dataset includes two wind speed conditions with 10-m equivalent wind speeds of $\overline{U}_{10} \approx 3.0$ and 6.0 m s^{-1} , respectively. The associated local wave ages were $C_p/\overline{U}_{10} \approx 0.6$ and 0.3. The wind-speed profiles were measured at a fetch of $x = 9.4$ m, using a TSI-8455-075-1 wind probe at heights from 5 cm to 13 cm and extrapolated to 10 m assuming neutral atmospheric conditions (see also §2 in Cao et al. (2026a)). In all campaigns, the breaking location was at about $x \approx 9.5$ m.

2.3 Measurements

With regard to measurements relevant to the present study, the evolution (surface elevation) of propagating wave groups upstream and downstream of the breaking region was recorded using an array of drop-down type, resistive wave gauges, sampling at 128 Hz. A total of 14 gauges were deployed in the *SIREN* campaign, and 16 gauges in the *BUBER* and *EURUS* campaigns. No wave gauges were placed within the immediate breaking region. Instead, the breaking process itself, together with its upstream and downstream spatial extent, was captured using three side-view digital cameras. Image sequences were recorded at 52 Hz for *SIREN* and at 20 Hz for *BUBER* and *EURUS*, covering a streamwise distance of approximately 4.5 m, from $x \approx 8.0$ to 12.5 m.

Image-processing tools developed in Cao et al. (2025) (CMG) and in Cao et al. (2026a) (SDBW-I) were employed to extract the spatial profile of the free surface at incipient breaking. This measurement is essential for determining the local wave steepness, which will be defined in §4.1.1. In addition, a hydrophone operating at a sampling frequency of 250 kHz was installed

beneath the breaking region to record acoustic emissions associated with bubble activities. Following established approaches (Deane and Stokes, 2002; Drazen et al., 2008; Sinnis et al., 2021; Zou et al., 2022), the acoustic records were processed to identify the duration τ_b over which breaking remained acoustically active. Details of the hydrophone signal processing procedure are provided in Cao et al. (2026b). This timescale was subsequently used in conjunction with the breaking-induced energy loss, ΔE_{br} , to infer the corresponding energy dissipation rate, ϵ_b (as detailed in §4.2.1).

3 Methods quantifying breaking-induced energy dissipation in laboratory flumes

Approaches used to quantify the energy dissipated by individual breaking waves, ΔE_{br} , in finite-width, unidirectional laboratory wave flumes have been varied across the literature. In this section, we consider three representative methods, proposed by Drazen et al. (2008), Tian et al. (2010) (building on earlier ideas by Banner and Peirson (2007)), and Cao et al. (2023), hereafter referred to as D08, T10, and C23.

The D08 method employs a control volume framework to estimate the loss of wave energy associated with breaking, within which background dissipation (e.g. viscous losses due to flume sidewall frictions) is implicitly accounted for. As discussed in Cao et al. (2023), however, the treatment of background energy losses in this approach is approximate and may lead to systematic overestimations in the values ΔE_{br} computed. The T10 method adopts a different strategy, in which a dense array of wave gauges distributed along the flume is used to directly characterise the evolution of wave energy and associated background dissipation. However, it requires extensive instrumentation and may not always be practical to implement, depending on the experimental configuration. Building on the control volume framework of D08, C23 revisited the representation of background dissipation and introduced a physically motivated correction that improves the accuracy of ΔE_{br} calculations.

In the following, we comment on these existing approaches and their underlying assumptions, before introducing a refined framework based on C23 that is adopted in the present study.

3.1 General framework for wave energetics and breaking-induced energy dissipation

In quantifying the amount of energy dissipated by wave breaking in unidirectional wave groups, one first considers the local mechanical energy flux, $\mathcal{F}(x, z, t)$ (units: $\text{J m}^{-2} \text{s}^{-1}$), through vertical sections at different streamwise locations along the wave flume. This flux represents the rate at which mechanical energy is transported in the streamwise direction, including contributions from kinetic energy, gravitational potential energy and pressure work. Mathematically, it may be expressed as

$$\mathcal{F}(x, z, t) = \left(\frac{1}{2} \rho_w \mathbf{U}^2 + \rho_w g z + \mathcal{P} \right) u_x, \quad (4)$$

where $\mathbf{U} = \sqrt{u_x^2 + u_z^2}$ is the magnitude of the fluid velocity, z denotes the vertical coordinate measured upward from the still water level, and \mathcal{P} is pressure. Hence, the two-dimensional total wave energy passing a given location x , $E(x)$ over a finite time interval ΔT , denoted as $E(x)$ (units: J m^{-1}), can then be written as the time-integrated, depth-integrated energy flux through that section,

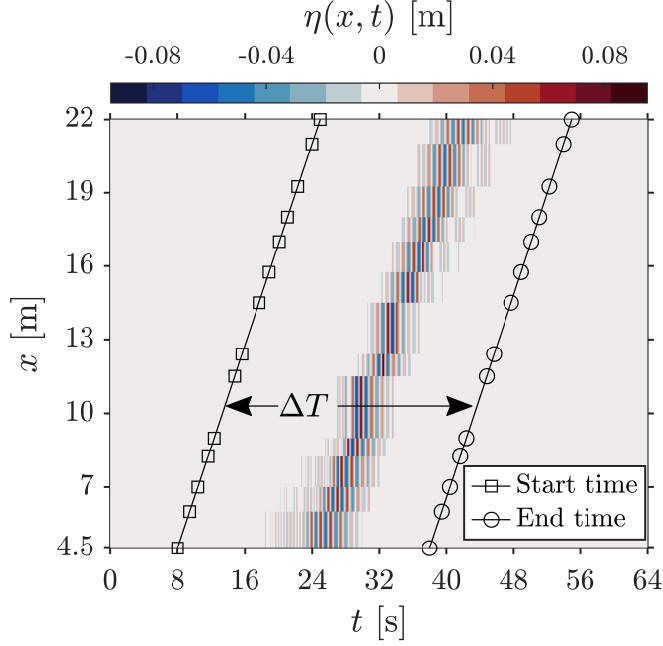


Figure 1. Illustration of the definition of the integration time window, $\Delta T = 30$ s, used in equation (6). The example shown corresponds to a wave group from the *SIREN* campaign with $\gamma = 2$, $T_p = 1.2$ s, and $A = 80$ mm. The time domain plotted covers the full 64 s repeat period, and the start and end times of the integration window are indicated, with squares and circles marking the streamwise locations of the 14 wave gauges used to measure the surface elevation. The integration window translates at a speed equal to the target wave group velocity, $C_{gp} = \partial\omega_p/\partial k_p = \omega_p(1 + 1.4k_p/\sinh(0.7k_p))/(2k_p)$, such that the entire wave group is captured as it propagates through the measurement array, while any contributions outside the window are excluded.

$$E(x) = \int^{\Delta T} \int_{-d}^{\eta} \mathcal{F}(x, z, t) dz dt = \int^{\Delta T} \int_{-d}^{\eta} \left(\frac{1}{2} \rho_w \mathbf{U}^2 + \rho_w g z + \mathcal{P} \right) u_x dz dt. \quad (5)$$

Under the assumptions of linear wave theory, for which the averaged depth-integrated kinetic and potential energy densities are assumed to be equal, $E(x)$ may be estimated from point measurements of the surface elevation time series, $\eta(x, t)$, according to

$$E(x) = \rho_w g \langle C_g \rangle(x) \int^{\Delta T} \eta^2(x, t) dt, \quad (6)$$

where $\langle C_g \rangle(x)$ represents a measure of the wave group velocity that is a function of space (Derakhti and Kirby, 2016; Xu et al., 2022; Cao et al., 2023). This equipartition assumption is valid only when the local non-linearity of the wave group remains sufficiently weak, and therefore equation (6) is not strictly applicable in the vicinity of focal or breaking locations, where non-linear effects become significant.

In the present study, $\langle C_g \rangle(x)$ in equation (6) was evaluated locally as a spectral-composition-weighted group velocity, following the approach originally proposed by Drazen et al. (2008) (see their equation (4.5)),

$$\langle C_g \rangle(x) \sim C_{gs}(x) = \frac{\sum_{i=1}^N C_{g,i} a_i^2 \delta f}{\sum_{i=1}^N a_i^2 \delta f}, \quad (7)$$

where $C_{g,i}$ represents the linear group velocity of the i th Fourier component. The integration duration ΔT in equation (6) was chosen as a fixed time window of 30 s (out of the full 64 s repeat period), which was sufficiently long to capture the entire propagating wave group at a given gauge while minimising contamination from reflected wave energy (see figure 1).

The total energy loss over the breaking process, ΔE , is obtained by considering a control volume between the inlet x_I and outlet x_O :

$$\Delta E = E(x_I) - E(x_O). \quad (8)$$

This total energy loss includes both breaking-induced dissipation (ΔE_{br}) and background dissipation (ΔE_{fr}) as previously mentioned, giving

$$\Delta E = \Delta E_{br} + \Delta E_{fr}. \quad (9)$$

Concatenating equations (8) and (9), the breaking-induced energy dissipation is therefore

$$\Delta E_{br} = E(x_I) - E(x_O) - \Delta E_{fr}. \quad (10)$$

For non-breaking wave groups, $\Delta E_{br} = 0$, and the total energy loss therefore reduces to the background dissipation, $\Delta E_{fr} = E(x_I) - E(x_O)$.

In laboratory wave flumes, background dissipation can represent a substantial fraction of the total energy loss. For example, [Banner and Peirson \(2007\)](#) reported that approximately 20% of the initial wave-group energy was dissipated over the propagation of non-breaking wave groups (see their figure 6). A comparable, though slightly smaller, fraction of about 15% was observed by [Cao et al. \(2023\)](#) in experiments conducted in the same flume as the present study. Unless the flume is sufficiently wide ([Zhang et al., 2019](#)), accurate quantification of ΔE_{fr} is therefore essential for reliably estimating the breaking-induced energy dissipation, ΔE_{br} . In the following, we revisit and assess the treatments of ΔE_{fr} and the corresponding estimates of ΔE_{br} adopted in D08, T10, and C23.

3.2 Existing methods used to quantify breaking wave energy dissipation in laboratory

3.2.1 Revisiting the T10 framework

The method proposed by [Tian et al. \(2010\)](#) estimates the breaking-induced energy dissipation by analysing the spatial evolution of the wave energy $E(x)$ along the flume. For non-breaking wave groups, $E(x)$ was shown to exhibit an exponential decay with distance that can be described by

$$E(x) = E_0 \exp(-\sigma_T x), \quad (11)$$

where $E_0 \simeq E(x_I)$ and σ_T is a spatial decay rate with units of m^{-1} . We illustrate the applicability of equation (11) to non-breaking wave groups in figure 2, where $E(x)$ decays in a manner that is well described by the exponential form. We also show linear fits for comparison, and note that, over the present measurement range, they are nearly indistinguishable from the exponential fits, consistent with [Tian et al. \(2010\)](#).

When wave breaking occurs, the T10 method applies two separate exponential fits of the form given in equation (11) to the data points upstream and downstream of an identified breaking location, x_b , in recognition of the different spatial decay behaviour before and after breaking. This procedure is demonstrated in figure 2 using two representative breaking wave groups, for which a distinct drop in $E(x)$ at x_b is observed (linear fits are again shown for visual comparison

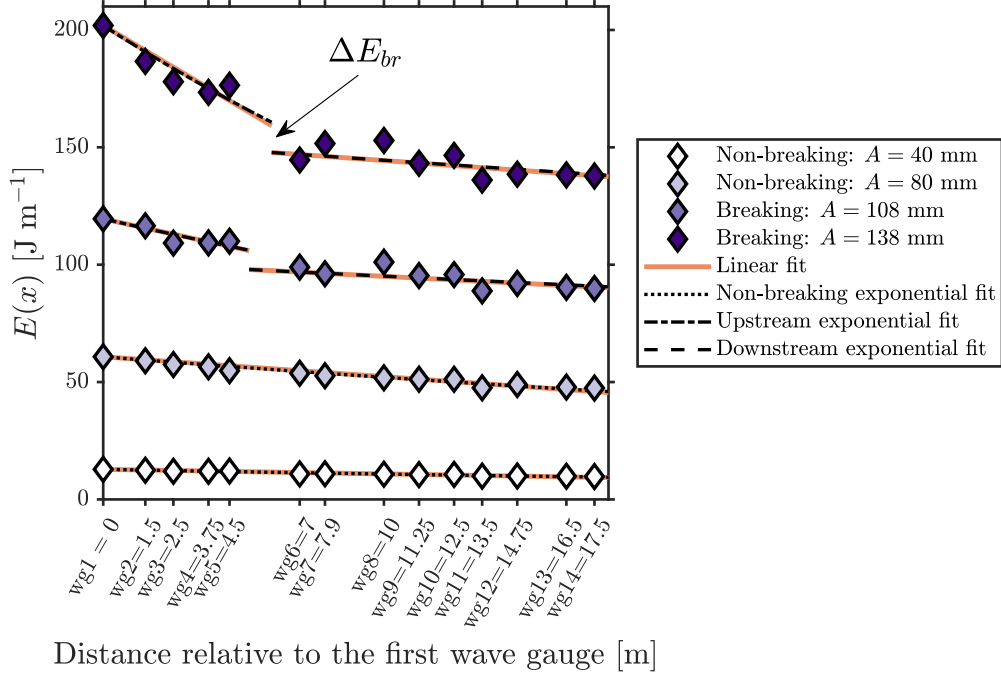


Figure 2. Illustration of the T10 framework applied to two sets of *SIREN* wave groups with $\gamma = 2$ and $T_p = 1.3$ s, including two non-breaking and two breaking cases. The wave gauge locations are shown as relative distances from wave gauge 1. Exponential fits following equation (11) are applied to the spatial evolution of $E(x)$. For breaking cases, separate fits are performed upstream and downstream of the identified breaking location x_b , and the breaking-induced energy dissipation, ΔE_{br} , is evaluated from the difference between the two fits at x_b . For comparison, linear fits (orange lines) are also shown.

and remain close to the exponential fits over the fitted ranges). The breaking-induced energy dissipation ΔE_{br} is then evaluated as the magnitude of this drop.

What becomes apparent is that only a single location x_b is considered in the T10 method in inferring ΔE_{br} . In practice, however, wave breaking occurs over a finite distance and the T10 method may underestimate ΔE_{br} for breaking events with a substantial extent. Also, the method requires a relatively dense spatial distribution of wave gauges in order to reliably constrain the energy decay before and after breaking; for example, the original study of [Tian et al. \(2010\)](#) employed approximately 30 wave gauges along the flume. Finally, measurements taken in close proximity to the breaking region are not explicitly excluded, which may introduce biases associated with strong local non-linearity. Because ΔE_{br} is obtained from the difference between two fitted curves at x_b , estimates for weakly dissipative breaking events may be sensitive to fitting uncertainty and the choice of x_b .

3.2.2 Comparison of the methods used in D08 and C23

Both D08 and C23 estimate breaking-induced energy dissipation ΔE_{br} using a control-volume-based energy balance. The key difference between the two methods lies in their respective treatments of the background energy dissipation ΔE_{fr} . This difference is illustrated in figure 3 using selected *SIREN* wave groups with $T_p = 1.3$ s and $\gamma = 2$.

In the D08 method, ΔE_{fr} is assumed to be a constant value and is taken as the dissipation measured for the most energetic non-breaking wave group. In the present dataset, a clearly isolated most energetic non-breaking case is not available. We therefore approximate ΔE_{fr} in D08 by taking the value inferred from the C23 method at the average initial energy between the most energetic non-breaking and the least energetic breaking wave groups, as indicated by

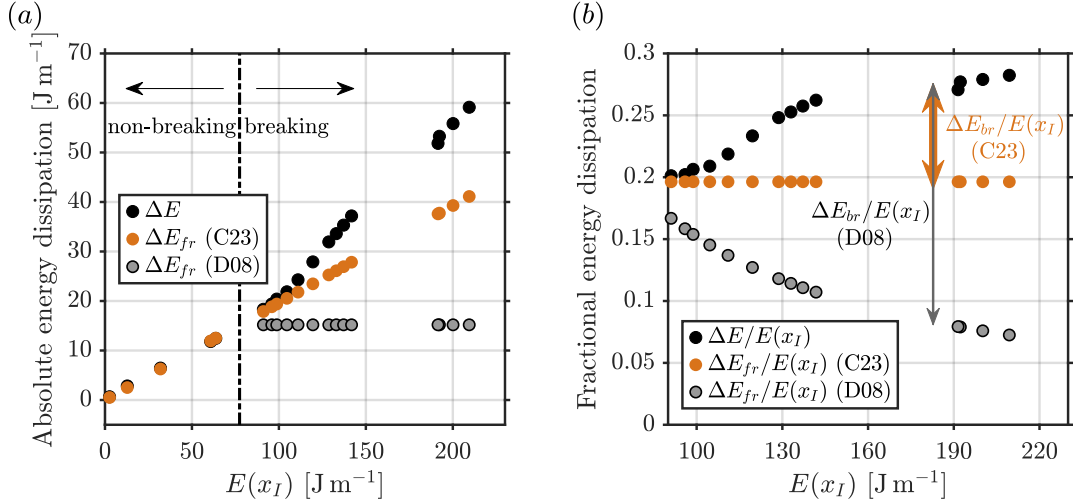


Figure 3. Comparison of the background energy dissipation (ΔE_{fr}) and breaking-induced energy dissipation (ΔE_{br}) quantified using the D08 and C23 methods for selected *SIREN* wave groups with $T_p = 1.3$ s and $\gamma = 2$. Panels (a) and (b) show the absolute and fractional energy dissipation, respectively, as functions of the upstream wave-group energy, $E(x_I)$. A range of $E(x_I)$ values between approximately 145 and 180 J m⁻¹ corresponds to cases with multiple breaking events and is therefore absent from the analysis. In applying the D08 method, ΔE_{fr} is approximated using the value inferred from the C23 method at the average $E(x_I)$ between the most energetic non-breaking and the least energetic breaking wave groups, as indicated by the vertical dot-dashed line in panel (a).

the vertical dot-dashed line in figure 3(a). As a result, the fractional background dissipation, $\Delta E_{fr}/E(x_I)$, given by the D08 method decreases with increasing wave group energy $E(x_I)$, as shown in figure 3(b).

In contrast, C23 demonstrated that ΔE_{fr} scales approximately linearly with $E(x_I)$, as indicated by the orange dots in figure 3(a). This is physically consistent with increased viscous and wall-related losses for more energetic wave groups (Perlin and Schultz, 2000). As a result, it is the fractional background dissipation, $\Delta E_{fr}/E(x_I)$, that remains approximately constant (figure 3b), and not its absolute value, ΔE_{fr} . Evidence for this can also be found in the original results of Drazen et al. (2008), whose figure 8 shows that the fractional energy loss of non-breaking wave groups remains largely unchanged with wave energy.

An underestimation of ΔE_{fr} in the D08 method consequently leads to an overestimation of the breaking-induced dissipation, ΔE_{br} , as illustrated in figure 3(b). On the other hand, C23 also noted that their formulation may slightly overestimate ΔE_{fr} , and thus underestimate ΔE_{br} , because ΔE_{fr} is related only to the upstream wave group energy $E(x_I)$. In practice, following breaking, a 'new' and less energetic wave group is formed downstream, which is expected to experience weaker background dissipation. This is consistent with the reduced spatial decay rates observed downstream of breaking in figure 2. In the next section, we describe how this effect is accounted for and introduce the refined framework adopted in the present study.

3.3 A refined framework based on C23

Notwithstanding the approximately linear relationship between the background dissipation ΔE_{fr} and the initial wave group energy reported in Cao et al. (2023) for non-breaking wave groups at a single characteristic scale ($T_p = 1.2$ s), this finding may no longer be appropriate when a broader range of underlying wave scales is considered. To verify this we quantify the total energy lost, ΔE , for all non-breaking wave groups in the *SIREN* dataset with T_p ranging from 1.0 to 1.6 s, and in this case $\Delta E_{fr} \equiv \Delta E$.

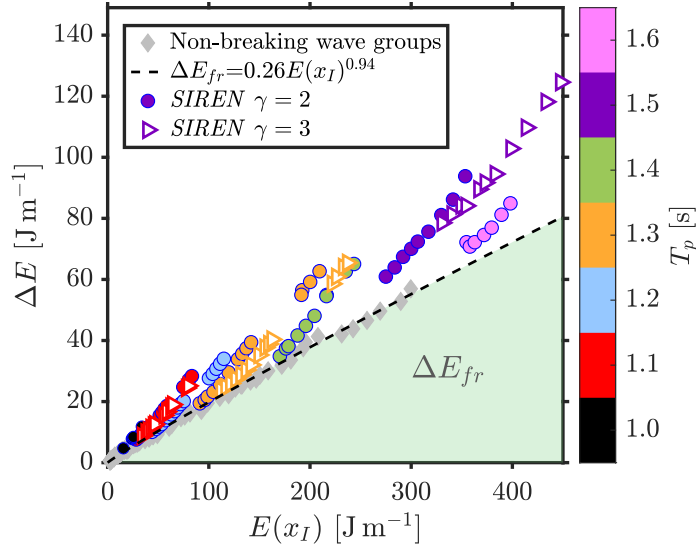


Figure 4. Total energy lost over the control volume quantified for all the *SIREN* wave groups plotted as a function of $E(x_I)$. Data points of different colours correspond to breaking wave groups with varying T_p . Non-breaking wave groups are shown as grey diamonds, while coloured symbols denote breaking cases. Fitting equation (12) to the non-breaking cases yields $\zeta_f = 0.26 \pm 0.02$ and $\nu_f = 0.94 \pm 0.015$, with a coefficient of determination $R^2 = 0.998$.

The resulting values of ΔE_{fr} are shown in figure 4, where non-breaking wave groups are indicated by grey symbols. When considered collectively across scales, the background dissipation is better described by a power-law relationship of the form

$$\Delta E_{fr} = \zeta_f E(x_I)^{\nu_f}, \quad (12)$$

where ζ_f and ν_f are empirical coefficients. A least-squares fit to the non-breaking wave groups shown in figure 4 yields $\Delta E_{fr} = 0.26 E(x_I)^{0.94}$. This constitutes the first modification to the C23 framework. Note that the values of ζ_f and ν_f are expected to depend on the specific characteristics of the wave flume (e.g. its geometry and boundary conditions) and the specific limits (x_I and x_O) defining the control volume.

Having established this improved semi-empirical method for estimating the total background energy dissipation in non-breaking wave groups, we now want to implement this to obtain a better estimate of the breaking-induced dissipation, ΔE_{br} , through a segmented analysis within the control volume defined. A schematic illustration of this framework is provided in figure 5(a), and it is achieved as follows.

We first consider a wave group entering the control volume at x_I with an initial energy $E(x_I)$. As the wave group propagates through the control volume, its energy decreases due to background dissipation, as observed for non-breaking wave groups (Tian et al., 2008, 2010) and confirmed in the present experiments (see figure 2 for both of our breaking and non-breaking cases). Given that equation (12) represents the total background energy dissipation over the full control volume, we define a constant background energy loss per unit length, which leads to the following differential form for the spatial change of the wave group energy:

$$\frac{dE}{dx} = -\frac{\zeta_f}{\Delta x} E(x_I)^{\nu_f}, \quad (13)$$

where Δx is the streamwise length of the control volume.

By doing so, the total background dissipation upstream of breaking can be quantified following (13) as $\Delta E_{fr,u} = [\zeta_f E(x_I)^{\nu_f} / \Delta x] \Delta x_u$, where $\Delta x_u = x_{b1} - x_I$ is the upstream distance

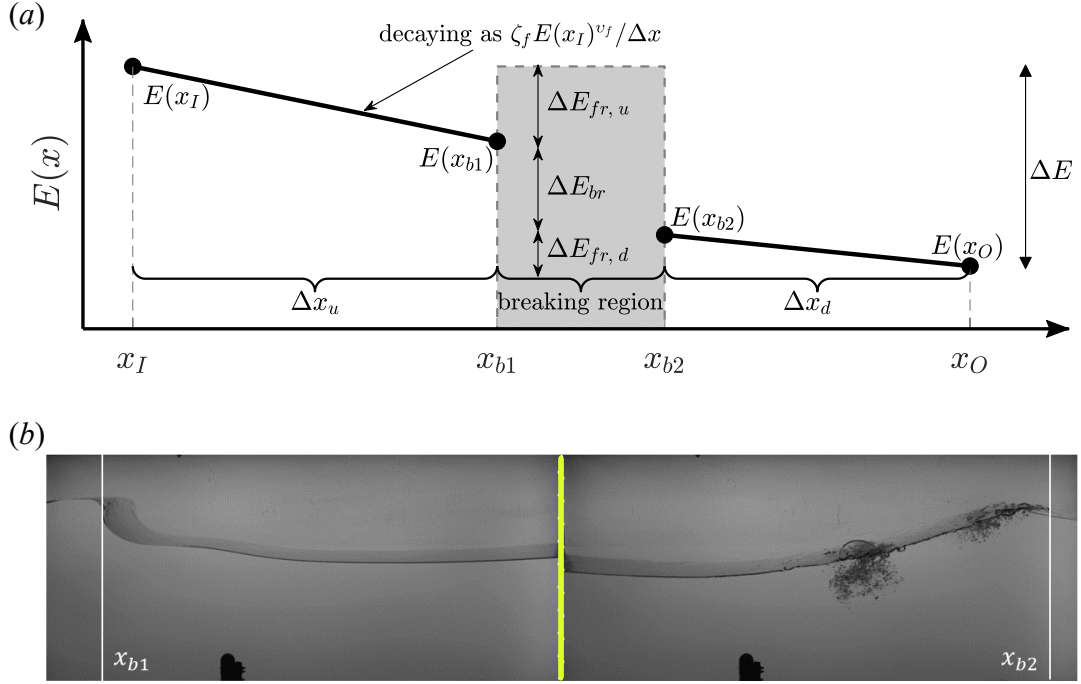


Figure 5. (a) Schematic illustration of the evolution of the wave energy $E(x)$ within the control volume in the presence of wave breaking. $E(x_{b1})$ and $E(x_{b2})$ denote the wave-group energy at the locations of incipient breaking (x_{b1}) and at the end of the breaking region (x_{b2}), respectively. The control volume is divided into three streamwise segments: an upstream region of length Δx_u , the breaking region between x_{b1} and x_{b2} , and a downstream region of length Δx_d . The total energy loss over the control volume, ΔE , is decomposed into upstream background dissipation $\Delta E_{fr,u}$, downstream background dissipation $\Delta E_{fr,d}$, and breaking-induced dissipation ΔE_{br} , such that $\Delta E = \Delta E_{fr,u} + \Delta E_{fr,d} + \Delta E_{br}$. The background energy dissipation implied by equation (12) per unit length is indicated schematically as $\zeta_f E(x_I)^{\nu_f} / \Delta x$ upstream of breaking, as explained in (13). (b) Snapshots of a single breaking event at (left) incipient breaking and (right) the end of breaking determined by hydrophone measurements. The vertical white lines indicate the locations of x_{b1} and x_{b2} .

over which background dissipation acts prior to breaking, such that the wave group energy at the location of incipient breaking becomes

$$E(x_{b1}) = E(x_I) - \Delta E_{fr,u} = E(x_I) \left(1 - \frac{\zeta_f}{\Delta x} E(x_I)^{v_f-1} \Delta x_u \right) \quad (14)$$

As depicted in figure 5(a), post the breaking process, a truncated, non-breaking wave group is formed downstream of the breaking region, with an energy level $E(x_{b2}) < E(x_{b1})$ at the end of breaking (x_{b2}). Because the location x_{b2} varies between breaking events and does not coincide with a fixed position of the wave gauge, direct measurements of $E(x_{b2})$ are generally not possible and thus $E(x_{b2})$ remains unknown. This is unlike the upstream segment, where the entering energy $E(x_I)$ is explicitly measured by wave gauges and can therefore be used directly can therefore be used directly via equation (13) to quantify the upstream background dissipation. An explicit estimate of $E(x_{b2})$ is therefore required in order to determine both the downstream background dissipation and the breaking-induced energy dissipation. To achieve this, and to obtain a closed expression for $E(x_{b2})$ from known quantities, we revert, for the downstream segment, to the underlying variable-dependent power law form implied by equation (13), and apply separation of variables between x_{b2} and x_O to infer $E(x_{b2})$ from the measured value at x_O . Introducing \tilde{E} as the integration variable, to distinguish it from $E(x_{b2})$ and the energy level at the outlet of the control volume $E(x_O)$, yields

$$\int_{E(x_{b2})}^{E(x_O)} \frac{1}{\tilde{E}^{v_f}} d\tilde{E} = -\frac{\zeta_f}{\Delta x} \int_{x_{b2}}^{x_O} dx = -\frac{\zeta_f}{\Delta x} \Delta x_d, \quad (15)$$

which then leads to

$$E(x_{b2}) = \left[E(x_O)^{1-v_f} + (1-v_f) \frac{\zeta_f}{\Delta x} \Delta x_d \right]^{\frac{1}{1-v_f}}, \quad (16)$$

where $\Delta x_d = x_O - x_{b2}$ is the downstream distance over which background dissipation acts after breaking. The downstream background dissipation $\Delta E_{fr,d}$ is then obtained simply as the difference between inferred energy level $E(x_{b2})$ given by (16) and the energy level measured at the outlet $E(x_O)$.

With the background dissipation decomposed into upstream and downstream contributions (i.e. $\Delta E_{fr} = \Delta E_{fr,u} + \Delta E_{fr,d}$; see also figure 5a), the breaking-induced energy dissipation within the control volume can be calculated from the energy balance in equation (10) as

$$\Delta E_{br} = E(x_I) - E(x_O) - (\Delta E_{fr,u} + \Delta E_{fr,d}), \quad (17a)$$

$$= E(x_{b1}) - E(x_{b2}), \quad (17b)$$

$$= E(x_I) \left(1 - \frac{\zeta_f E(x_I)^{v_f-1}}{\Delta x} \Delta x_u \right) - \left[E(x_O)^{1-v_f} + (1-v_f) \frac{\zeta_f}{\Delta x} \Delta x_d \right]^{\frac{1}{1-v_f}}. \quad (17c)$$

In (17b), $E(x_{b1})$ and $E(x_{b2})$ are given by equations (14) and (16), respectively. The final expression (17c) enables ΔE_{br} to be estimated using surface elevation measurements at the two fixed locations x_I and x_O defining the control volume, alongside the breaking locations x_{b1} and x_{b2} determined from side-view imagery.

Within the refined framework, the location x_{b1} is defined as the point at which the wave crest first becomes vertical at incipient breaking, coinciding with the onset of imminent overturning (Deike et al., 2015). The downstream limit of the breaking region, x_{b2} , is defined as the location of the downstream end point of the breaking-induced disturbance when active breaking ceases.

Representative examples illustrating the identification of x_{b1} and x_{b2} are shown in the snapshots in figure 5(b). These locations are converted into physical coordinates using the real-world conversion procedure described in Cao et al. (2025). We assess the performance of the refined framework through direct comparison with the methods of D08, T10 and C23 in Appendix A, and show that the maximum values of the breaking-induced fractional dissipation $\Delta E_{br}/E(x_I)$ obtained using the present framework can be about 10% lower than those inferred using the D08 method.

It should be noted that in our refined framework the background dissipation occurring within the breaking region itself is neglected. This assumption is adopted due to the relatively short spatial extent of the breaking region compared to the full scale of the control volume, $|x_{b1} - x_{b2}| \ll |x_I - x_O|$. Indeed, across all breaking events examined here, the maximum breaking length was observed to be $|x_{b1} - x_{b2}|_{\max} \sim \mathcal{O}(10\%)|x_I - x_O|$, while ΔE_{br} contributes only $\mathcal{O}(1\%)$ to the total breaking-induced energy dissipation. An additional source of uncertainty when using equation (17c) arises from the identification of x_{b1} and x_{b2} which can be subjective. We conduct a sensitivity test in Appendix B, and the results demonstrate that reasonable variations in the selection of x_{b1} and x_{b2} do not critically affect the resulting estimates of ΔE_{br} .

4 Results and discussions

4.1 Breaking-induced energy dissipation ΔE_{br}

4.1.1 Definitions and implications of wave group steepness and local steepness

As wave steepness \mathcal{S} is an important variable controlling breaking-induced energy dissipation, we begin by clarifying the two types of wave steepness employed here to investigate the influence that wave scale and direct wind forcing have on the energy dissipated by wave breaking.

The first type of \mathcal{S} is based on the spectral behaviour of the propagating wave group and is evaluated using surface elevation time-series measured at a fixed location upstream of breaking. As such, this wave group steepness characterises the state of the wave field prior to breaking and serves as a predictive metric, providing a means by which the threshold condition for breaking onset¹ and the associated crest steepness at incipient breaking may be inferred (McAllister et al., 2024; Cao et al., 2026a).

One wave group steepness measure of this type is \mathcal{S}_n , which is defined earlier by (3). The value of \mathcal{S}_n is very sensitive to local non-linear changes in the wave spectrum and therefore depends on the location at which it is evaluated relative to the breaking point (Cao et al., 2026a). This motivates the use of an alternative wave group steepness measure defined in a spectrally energy-weighted manner (Tian et al., 2010; Derakhti and Kirby, 2016),

$$\mathcal{S}_s = k_s \sum_{i=1}^N a_i, \quad \text{where} \quad \begin{cases} k_s \equiv k(f_s), & \text{from the linear dispersion relation,} \\ f_s = \frac{\sum_{i=1}^N f_i a_i^2}{\sum_{i=1}^N a_i^2}, \end{cases} \quad (18)$$

because it was shown to better capture the breaking onset threshold and to be much less sensitive to the measurement location as the wave spectrum evolves non-linearly (Cao et al., 2023, 2026a). In the present study both wave group steepness measures \mathcal{S}_n and \mathcal{S}_s are quantified at the inlet of the control volume (x_I) where we assume that wave group non-linearity remains

¹In the present work, the breaking onset threshold refers to a (geometric, kinematic, or dynamic) limiting condition under which the least energetic breaking can be triggered, and is distinguished from incipient breaking which represents the instant at which the local crest is about to break.

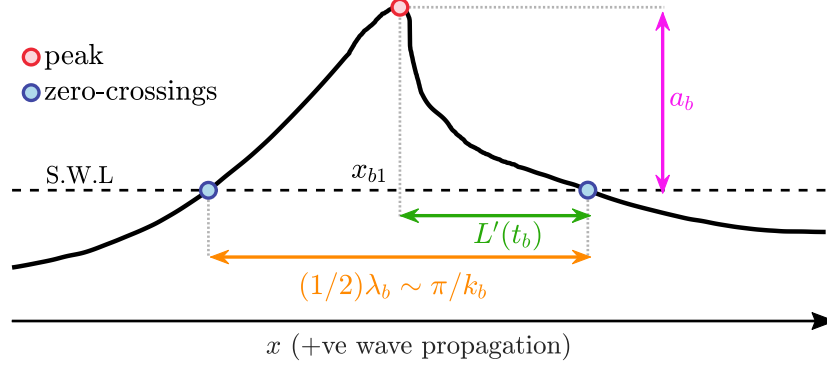


Figure 6. Demonstration of the spatial parameters characterising the crest profile at incipient breaking (t_b).

weak.

The second type of steepness directly quantifies the local crest geometry at incipient breaking and therefore reflects the cumulative effects of non-linear wave evolution, energy focusing and wind forcing acting up to the breaking point. This type is here referred to as local steepness. Following previous studies (e.g. Tian et al., 2008; Saket et al., 2017; Derakhti et al., 2018; De Vita et al., 2018; Touboul and Banner, 2021), the first measure of local steepness we use is defined as

$$\mathcal{S}_b = a_b k_b \equiv a_b \pi \left(\frac{1}{2} \lambda_b \right)^{-1}, \quad (19)$$

where a_b is the local crest amplitude at incipient breaking, λ_b is the local wavelength estimated by doubling the zero-crossing distance (see figure 6) from which the local wavenumber, k_b , is calculated in the usual way.

Several relevant studies have suggested that the steepness of the crest front provides a more effective description of both the breaking onset and the limiting local crest form immediately prior to breaking (Perlin et al., 2013; McAllister et al., 2023; Cao et al., 2026a). Accordingly, we employ a second local steepness measure defined at incipient breaking as

$$\mathcal{S}_{\text{front}}(t_b) = \frac{a_b}{L'(t_b)}, \quad (20)$$

where $L'(t_b)$ is the instantaneous horizontal length of the crest front at the time of incipient breaking t_b , as is illustrated in figure 6.

4.1.2 Breaking-induced fractional energy dissipation at different wave scales

The energy dissipation of breaking waves under varying wave scales is examined here by plotting $\Delta E_{br}/E(x_I)$ against different measures of wave group steepness and local steepness defined in equations (3), (18), (19) and (20). The results are presented in figure 7 for *SIREN* (unforced) breaking wave groups with varying peak periods T_p (and γ), for which $\Delta E_{br}/E(x_I)$ is found to lie in the range of approximately 0.01–0.13.

A similar dependence between $\Delta E_{br}/E(x_I)$ and wave group steepness measures, $\mathcal{S}_n(x_I)$ and $\mathcal{S}_s(x_I)$, is found (figures 7a, b): increasing T_p is associated with both a higher steepness threshold for breaking onset and a steeper increase of $\Delta E_{br}/E(x_I)$ with increasing wave group steepness. The combined effect of these two trends makes the influence of wave scale on energy dissipation difficult to characterise at any single wave group steepness value. In previous work, Cao et al. (2023) demonstrated that the influence of spectral bandwidth on energy dissipation could be

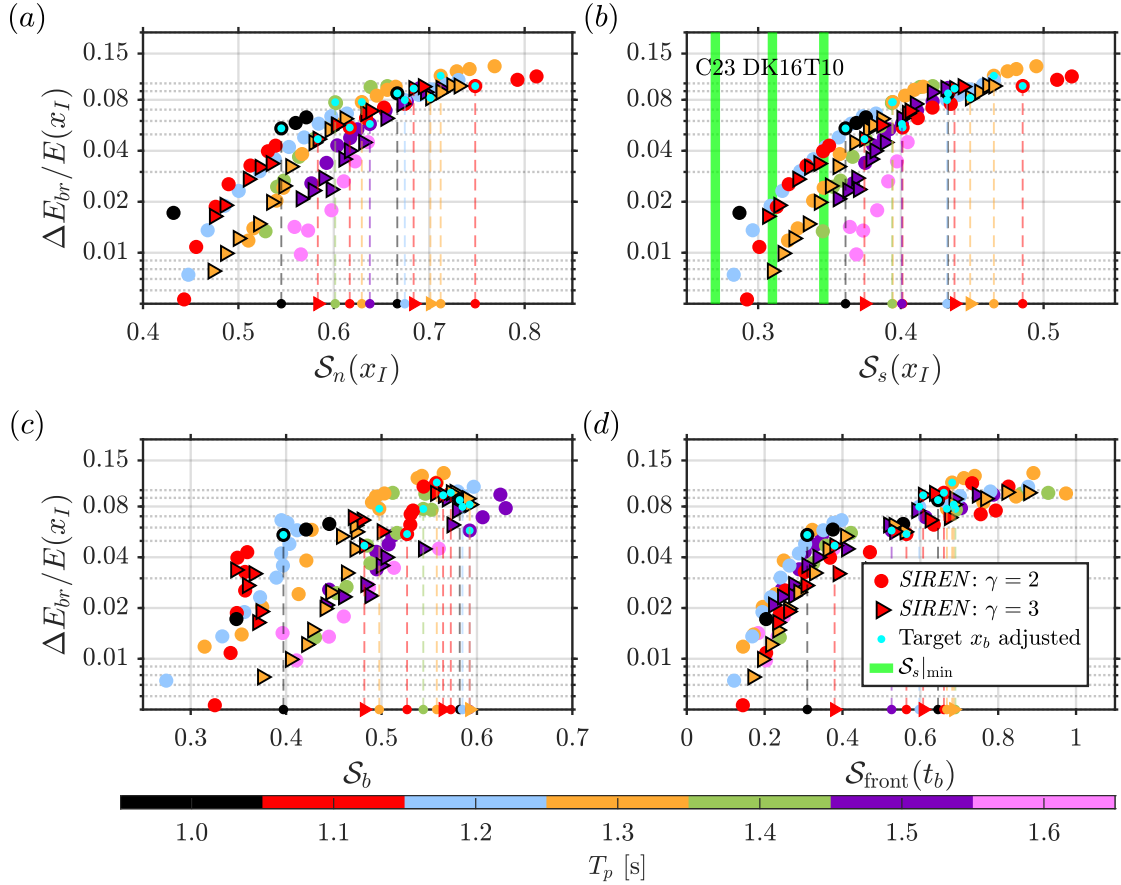


Figure 7. Breaking-induced fractional energy dissipation $\Delta E_{br}/E(x_I)$ plotted as functions of various measures of wave (group) steepness for *SIREN* breaking waves: panels (a, b) use spectral measures representing wave group steepness and panels (c, d) use two locally-defined steepness measures at incipient breaking. Vertical green lines in (c) indicate the breaking-onset threshold steepness identified by C23 (Cao et al., 2023), T10 (Tian et al., 2010), and DK16 (Derakhti and Kirby, 2016). Data points marked by cyan dots correspond to cases in which the wave that actually breaks differs from the target focused wave within the group. In these cases, the target breaking location x_b is adjusted to ensure that the individual breaking event occurs within the camera measurement region. The dashed lines connect these data points to their corresponding S values on the abscissa.

largely mitigated by using the spectrally-weighted steepness $\mathcal{S}_s(x_I)$, arguing explicitly that $\mathcal{S}_s(x_I)$ unifies the breaking-onset condition across different bandwidths (see the green vertical lines in figure 7*b*). This is, however, not observed here for breaking waves with different T_p , indicating that wave group steepness alone is insufficient to characterise breaking-induced energy dissipation across different wave scales (even when ΔE_{br} is normalised by the incoming wave group energy). This highlights the limitations in extrapolating results derived at a given scale to a larger range of scales and supports the investigation of a range of scales where practically possible.

This limitation is not removed either when using the local steepness based on zero-crossing analysis \mathcal{S}_b (c.f. (19)), as shown in figure 7*c*). Results corresponding to different wave scales are separated, and an apparent saturation behaviour of \mathcal{S}_b is observed, whereby further increases in $\Delta E_{br}/E(x_I)$ are not accompanied by a corresponding increase in \mathcal{S}_b .

By contrast, a substantial reduction in the scatter, and hence in the apparent wave-scale dependence, is obtained when we use the crest-front steepness $\mathcal{S}_{\text{front}}(t_b)$ (figure 7*d*), as defined by (20). This can be attributed in large part to the ability that $\mathcal{S}_{\text{front}}(t_b)$ has to account more accurately for breaking onset for (unforced) breaking waves (Cao et al., 2026a).

Among many previous studies (e.g. Cao et al., 2023), we note also in our present experiments that in dispersively-focused wave groups continuing to increase the focusing amplitude A may lead to breaking events with multiple breaking waves, before the isolated breaking can be reproduced with further increase in A . In the latter case, the wave that actually breaks may differ from the target focused wave within the wave group. In the present study, only isolated breaking events are retained, and cases for which a shift in the breaking wave occurs are marked in figure 7 using cyan dots. This shift may contribute, at least in part, to the appearance of two data clusters separated at approximately $\mathcal{S}_{\text{front}}(t_b) \approx 0.5$ in figure 7*d*).

4.1.3 Breaking-induced fractional energy dissipation at different co-flowing wind speeds

We now explore the influence that co-flowing wind has on breaking-induced energy dissipation. We recall that the wave group steepness measures, $\mathcal{S}_n(x_I)$ and $\mathcal{S}_s(x_I)$, are evaluated upstream of the breaking region at small fetch and therefore remain largely independent of the applied wind forcing. As such, these steepness measures provide a reasonable reference for isolating wind effects on $\Delta E_{br}/E(x_I)$ when comparisons are made with the corresponding unforced cases.

Figure 8 presents the relationship between $\Delta E_{br}/E(x_I)$ and wave steepness under different wind conditions using data from the *BUBER* (no wind) and *EURUS* (characterised by wave ages $C_p/\overline{U}_{10} \approx 0.6$ and 0.3) campaigns. A key point to note first is that for a given wave group steepness, the presence of wind tends to lower the fractional energy dissipation of individual breaking waves (figures 8*a* and *b*). This reduction becomes more pronounced as the wind speed increases (corresponding to decreasing C_p/\overline{U}_{10}). This also appears to be true when the local steepness \mathcal{S}_b is considered (figure 8*c*).

There is no single mechanism through which the wind-induced reduction in $\Delta E_{br}/E(x_I)$ can be explained. Instead, the observed decrease may arise from a combined consequence of wind-induced changes in wave dispersion, high-frequency spectral energy content, and aerodynamic sheltering effects (Cao et al., 2026a), all of which influence how waves break. From the perspective of crest-front geometry at incipient breaking, however, recent observations by Cao et al. (2026a) indicate that wind-forced breaking tends to occur at smaller crest-front steepness values due to reduced forward leaning of the crest (n.b. this is consistent with the earlier breaking inception inferred by Boettger et al. (2024) based on energetic arguments). One may therefore expect part of the apparent wind-induced reduction in $\Delta E_{br}/E(x_I)$ to be compensated when

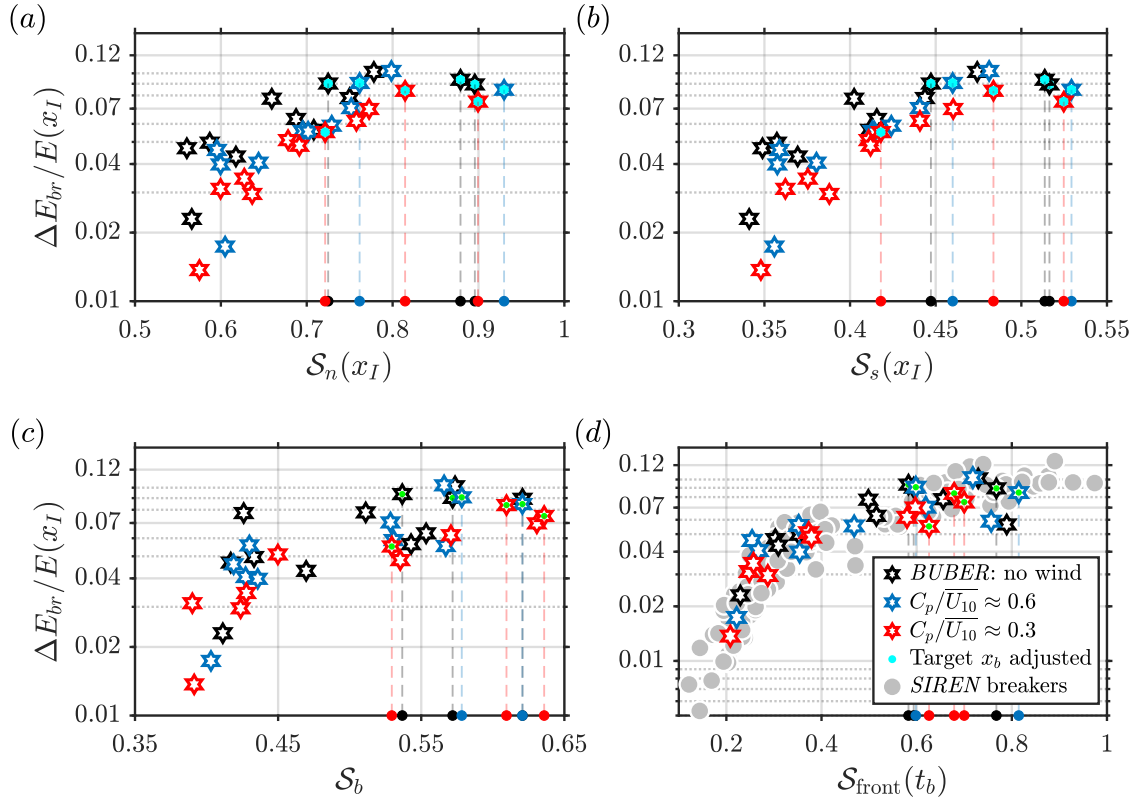


Figure 8. As of figure 7 but now for breaking waves from *BUBER* (no wind) and *EURUS* ($C_p/\overline{U}_{10} \approx 0.6$ and 0.3) datasets. Results from *SIREN* are shown as background data in (d) for comparison.

the local crest-front shape is taken into account. Indeed, when we use $\mathcal{S}_{\text{front}}(t_b)$ the influence of wind forcing is largely removed (figure 8d), and the wind-forced cases follow trends that are consistent with the wind-unforced data (including those from *SIREN* shown in the background in figure 8d as grey circles).

4.1.4 Subsection summary

Taken together, we may conclude so far from §4.1.2 and §4.1.3 that the way through which wave scale and direct wind forcing influence breaking-induced energy dissipation can be understood in terms of their respective effects on the breaking onset threshold (determined by wave group steepness) and on the local crest geometry at incipient breaking. Importantly, both effects are largely captured when the crest-front steepness $\mathcal{S}_{\text{front}}(t_b)$ is employed.

This finding is consistent with the working hypothesis put forward in Cao et al. (2026a), namely that when using wave steepness as the only controlling variable, $\mathcal{S}_{\text{front}}(t_b)$ provides the most effective description of breaking-induced energy dissipation among the wave steepness measures examined. In the following sections where we examine the energy dissipation rate this finding will be used to help develop an alternative scaling for $\Delta E_{br}/E(x_I)$ (§4.3).

4.2 Energy dissipation rate ϵ_b

4.2.1 Choice of active breaking timescale and its visual interpretation

As introduced in §2.3, we quantify the rate at which wave energy is dissipated by breaking per unit crest length as

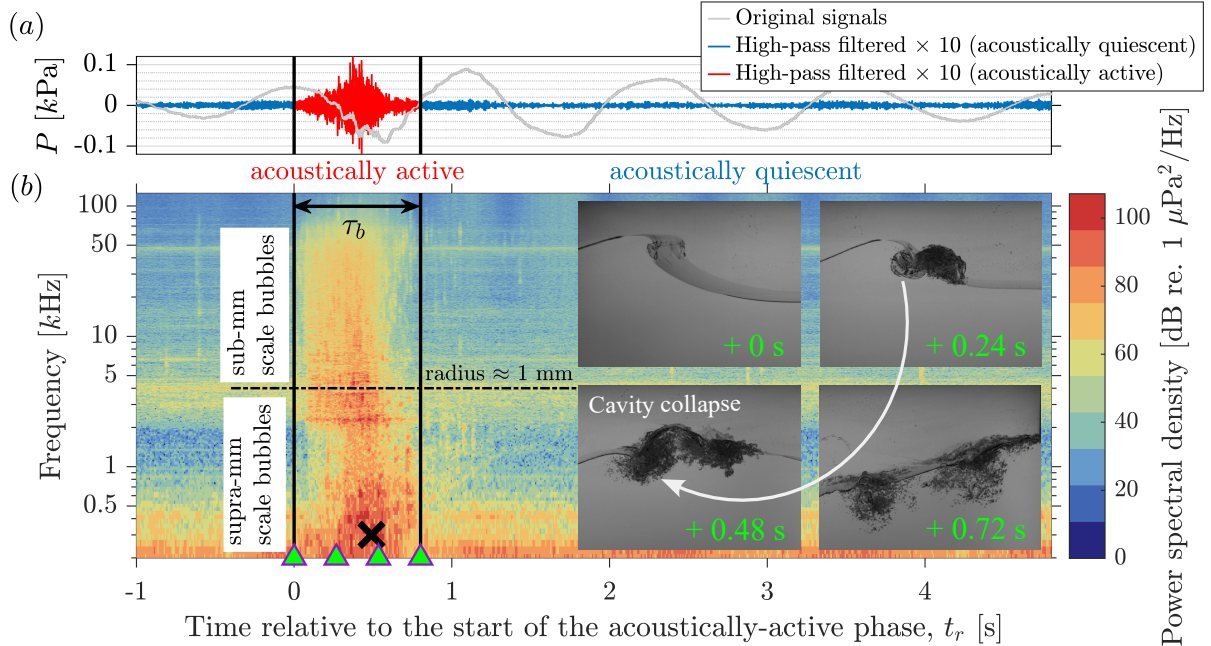


Figure 9. Illustration of the analysis of hydrophone acoustic outputs during a typical breaking event from the *SIREN* dataset ($\gamma = 3$, $T_p = 1.2$ s, $A = 110$ mm). (a) Original pressure time history and the corresponding signal after applying a 200 Hz high-pass filter (scaled by a factor of 10 for visual comparison). Region enclosed by the black lines denotes the acoustically-active phase with duration τ_b . (b) Spectrogram calculated from the high-pass filtered signals, with colour indicating the power spectral density (PSD) in dB referenced to $1 \mu\text{Pa}^2 \text{Hz}^{-1}$. Four green triangles along the time (horizontal) axis indicate the (evenly spanned) time sequence of the example images shown on the right, taken over the duration of active breaking. Black cross in the spectrogram marks the time and frequency at which the acoustic signal near 300 Hz reaches a maximum, corresponding to the breakup of the primary cavity (air pocket) entrained (Deane and Stokes, 2002; Gao et al., 2021). Horizontal dash-dotted line denotes the characteristic frequency associated with bubbles of radius 1 mm, separating the regimes dominated by supra-mm and sub-mm bubble activities.

$$\epsilon_b = \frac{\Delta E_{br}}{\tau_b}, \quad (21)$$

where τ_b is the duration of acoustically-active breaking inferred from hydrophone measurements. Following the procedure described in Cao et al. (2026b), we process the raw hydrophone voltage signals using a 200 Hz high-pass filter to isolate the acoustic emissions associated with bubble entrainment and break-up. Figure 9(a) shows an example of the original and filtered pressure time histories recorded during a typical breaking event.

The associated spectrogram calculated from the high-pass filtered signal is given in figure 9(b), in which the duration of the acoustically-active breaking τ_b can be clearly identified together with the frequency band over which acoustic emissions occur. We may divide the latter into regimes associated with the activity of supra-mm and sub-mm bubbles, respectively (Deane and Stokes, 2002; Gao et al., 2021), as shown by the horizontal dash-dotted line in figure 9(b).

To aid visual interpretation of the acoustically-active phase, we also attach in figure 9(b) a sequence of images with the sampling times indicated by the green triangles along the time axis. At the beginning of the acoustically-active phase ($t_r = 0$ s), the wave crest has already overturned and initial air entrainment is observed. This occurs later than the instant at which the crest front first becomes vertical (t_b), which we use to define incipient breaking. Between $t_r = 0.24$ s and $t_r = 0.48$ s, a pronounced peak is seen near 300 Hz in the spectrogram (marked by the black cross), corresponding to the collapse of the primary cavity where the air pocket

entrained is fragmented into smaller bubbles following a cascade process (Deane and Stokes, 2002; Gao et al., 2021; Liu et al., 2024; Qi et al., 2024). Towards the end of the acoustically-active phase ($t_r = 0.72$ s) the submerged bubble plume begins to disperse, air entrainment ceases and surface disturbances diminish.

It is worth noting that the timescale τ_b defined in the above manner is shorter than breaking durations typically inferred from side-view imagery based on visual assessment of the breaking process (Tian et al., 2010; Craciunescu and Christou, 2020; Cao et al., 2023), and longer than durations inferred from the growth of whitecap area in top-view imagery (Deane et al., 2016; Callaghan et al., 2016) by about 15% (Cao et al., 2026b). The reason we use τ_b to calculate energy dissipation rate in (21) is motivated by the following physical and practical considerations.

First, the energy dissipated by vorticity generated during the initial crest overturning prior to air entrainment, which is not included in τ_b , is considered to be small relative to the total energy loss over the entire breaking event (Derakhti and Kirby, 2014). The characteristic timescale of crest overturning is of order 0.1 s (Tian et al., 2012), and including this phase would therefore lead to a systematic underestimation of the energy dissipation rate. Second, determining the end of active breaking from imagery requires visual identification of the point at which surface disturbances fully subside, and such a procedure can introduce subjective bias, particularly for plunging events. In addition, the rise of bubble plumes from the water column can induce local surface agitation that further complicates such visual assessments. In this regard, the acoustically based definition of τ_b provides a more objective measure of the active breaking duration and therefore is preferred here.

4.2.2 Energy dissipation rates at varying breaking conditions

In figure 10, values of the breaking-induced energy dissipation rate ϵ_b computed using (21) are shown. Here, we focus on the wave group steepness $\mathcal{S}_s(x_I)$ and the crest-front steepness $\mathcal{S}_{\text{front}}(t_b)$, as these two measures were shown before in Cao et al. (2023) and in §4.1.1 to provide more consistent characterisation of breaking-induced energy dissipation. Since ϵ_b is a dimensional variable, an inherent dependence on the underlying wave scale can therefore be expected, as illustrated by the inset in figure 10(a). To account for this, we rescale ϵ_b by $E(x_I)^{-1} T_b$ but combine it with the steepness measures on the abscissa as independent variables.

From the left column panels of figure 10, ϵ_b is seen to correlate positively with $\mathcal{S}_s(x_I) E(x_I) T_b^{-1}$ across unforced laboratory conditions (*SIREN*, *BUBER*) as well as data we draw from literature (T10, DK16). The remaining scatter is potentially a consequence of the fact that $\mathcal{S}_s(x_I)$ does not fully capture the onset of breaking across self-similar conditions over a range of underlying wave scales (figure 10a). In addition, consistent with the behaviour observed for fractional energy dissipation in figure 8, imposing wind forcing is found to reduce the energy dissipation rate for similar wave group steepness (figure 10c).

A more striking result comes from the right column panels in figure 10 when we employ $\mathcal{S}_{\text{front}}(t_b)$ in place of $\mathcal{S}_s(x_I)$. In this scenario, values of ϵ_b from different wind speed and wave scale conditions appear to collapse considerably onto a common trend for which we may parameterise the dependence using a linear fit,

$$\epsilon_b = 0.14 (\pm 0.006) \mathcal{S}_{\text{front}}(t_b) \frac{E(x_I)}{T_b}, \quad (22)$$

with a coefficient of determination $r^2 = 0.87$ (blue lines in figures 10b and 10d). This means that once appropriately scaled the energy dissipation rate can be constrained effectively by the crest-front steepness, over the range of breaking conditions studied here.

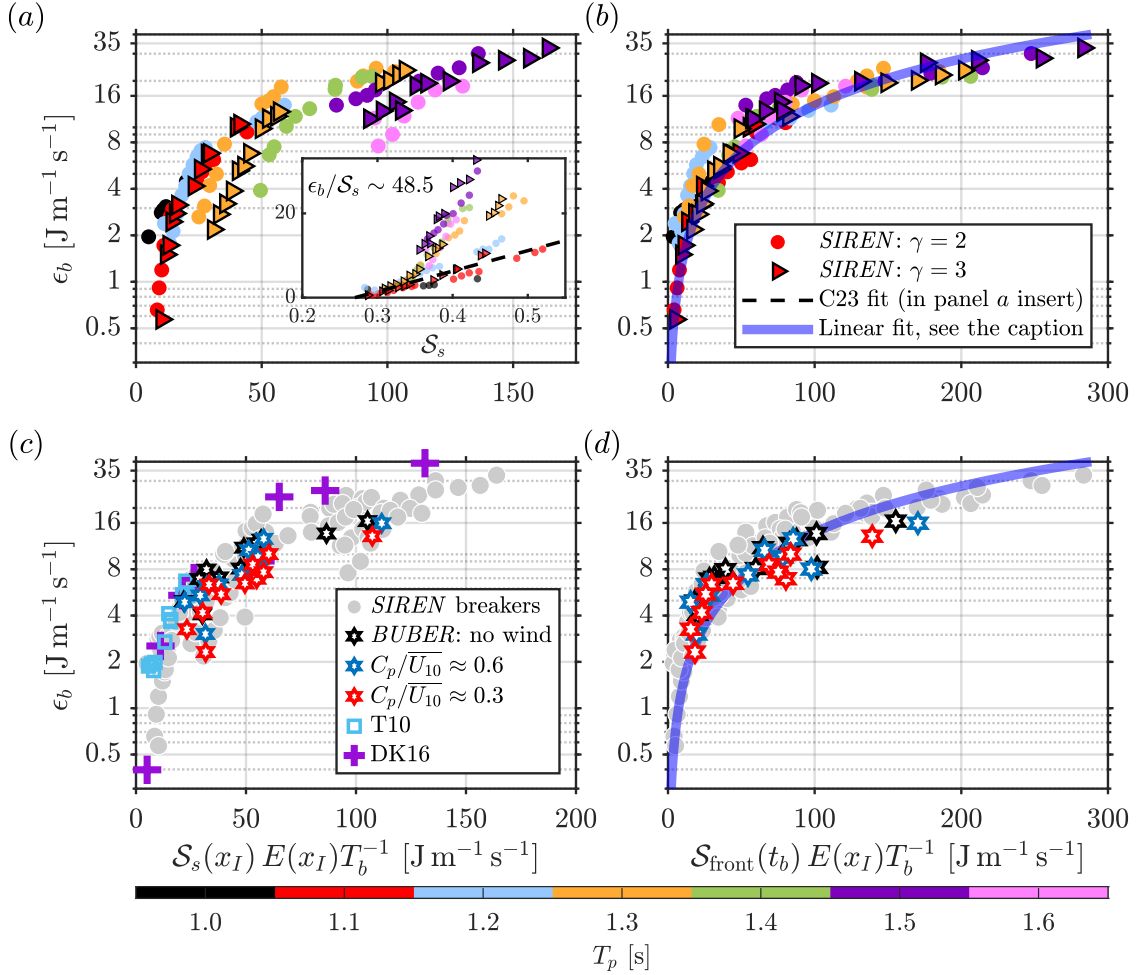


Figure 10. Energy dissipation rates of individual breaking waves ϵ_b plotted as a function of two \mathcal{S} measures where (a, c) $\mathcal{S}_s(x_I)$ and (b, d) $\mathcal{S}_{\text{front}}(t_b)$. In all panels, the steepness measures are rescaled by $E(x_I) T_b^{-1}$. Data from *SIREN* are shown in panels (a, b) and are included as background points in panels (c, d), where additional results from *BUBER*, *EURUS*, T10 (Tian et al., 2010), and DK16 (Derakhti and Kirby, 2016) are presented. The inset in (a) plots the values of ϵ_b with respect to $\mathcal{S}_s(x_I)$ without rescaling. Also shown is the empirical linear relationship reported by Cao et al. (2023), who obtained a gradient of $\epsilon_b/\mathcal{S}_s \sim 48.5$ for $T_p = 1.2$ s breaking waves. This appears, however, to align more closely with the $T_p = 1.1$ s cases shown here (red dots), reflecting the slightly different methods used to estimate energy dissipation (see appendix A). The blue lines in panels (b, d) denote linear best-fit relations given in (22).

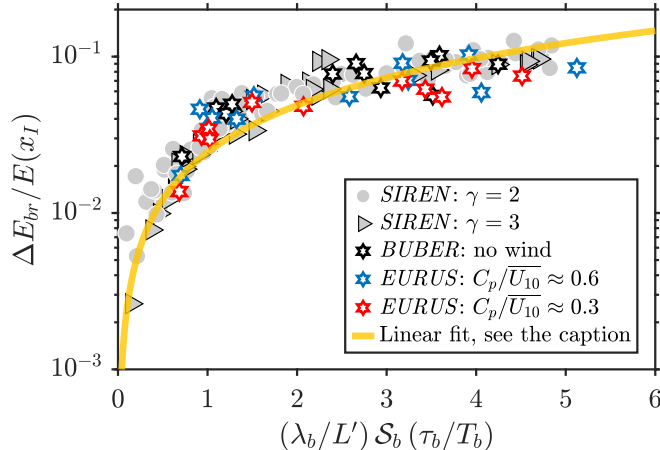


Figure 11. Comparison between fractional energy dissipation and the scaling set $(\lambda_b/L') \mathcal{S}_b(\tau_b/T_b)$ for all breaking waves from the *SIREN*, *BUBER* and *EURUS* datasets. The yellow line shows the linear best fit forced through the origin, with a gradient of $0.024(\pm 0.001)$ and $r^2 = 0.8$.

4.3 Discussion on the implications of $\mathcal{S}_{\text{front}}(t_b)$ and (22) for constraining $\Delta E_{br}/E_0$

As discussed in §4.1.4, among the various steepness measures considered, the crest-front steepness $\mathcal{S}_{\text{front}}(t_b)$ provides the most effective description of breaking-induced fractional energy dissipation. We understand this behaviour in terms of the way in which $\mathcal{S}_{\text{front}}(t_b)$ delineates both the breaking onset threshold and the local crest geometry at incipient breaking. By decomposing the definition of $\mathcal{S}_{\text{front}}(t_b)$ in (20), we may attribute its better performance, at least in part, to the fact that $\mathcal{S}_{\text{front}}(t_b)$ effectively serves as a bulk measure considering both the local non-linearity ($a_b k_b$, which is essentially S_b) and the fore–aft asymmetry of the crest $((k_b L')^{-1}$, see also figure 6).

For $\Delta E_{br}/E(x_I)$ to be parameterised by $\mathcal{S}_{\text{front}}(t_b)$, the threshold value associated with breaking onset must first be accounted for. The relevant independent variable is therefore expressed as $\mathcal{S}_{\text{front}}(t_b) - \mathcal{S}_{\text{front}}(t_b)|_{\text{onset}}$, consistent with the threshold correction later applied to the prediction of the breaking strength parameter (24) in §4.4. Applying this correction to the data in figure 8(d) gives $\Delta E_{br}/E(x_I) = 0.13(\pm 0.01) [\mathcal{S}_{\text{front}}(t_b) - \mathcal{S}_{\text{front}}(t_b)|_{\text{onset}}]$, with $\mathcal{S}_{\text{front}}(t_b)|_{\text{onset}} = 0.05(\pm 0.03)$ and $r^2 = 0.84$. This removal of the onset threshold follows the same rationale as the threshold corrections applied by Romero et al. (2012) and Sinnis et al. (2021) to steepness-based predictions of the breaking strength parameter.

On the other hand, if we combine the decomposition of $\mathcal{S}_{\text{front}}(t_b)$ shown above with the definition of the energy dissipation rate in (21) and its parametrised form in (22), we arrive at a more physically motivated scaling for the fractional energy dissipation:

$$\frac{\Delta E_{br}}{E_0} \sim \frac{\Delta E_{br}}{E(x_I)} \propto \frac{2\beta^*}{\pi} S_b \frac{\tau_b}{T_b}, \quad (23)$$

where $\beta^* = \lambda_b/(4L')$ is a crest-leaning parameter we define that equals unity for symmetric crests and increases as the crest leans forward in the event of breaking (i.e. L' decreases in relation to the full wavelength λ_b). The proportional relationship in (23) is verified in figure 11 using all the breaking waves from the *SIREN*, *BUBER*, and *EURUS* experiments, and is found to function well across the range of breaking conditions we explore (see the yellow line).

Equation (23) has important implications for what we presently understand about how $\Delta E_{br}/E_0$ is characterised by \mathcal{S} -based measures. In addition to local non-linearity and crest

asymmetry (which are naturally incorporated in the definition of $\mathcal{S}_{\text{front}}(t_b)$), it identifies the non-dimensional breaking duration τ_b/T_b as an additional controlling variable for fractional energy dissipation. Indeed, although assumptions have been taken to tie the (absolute) breaking duration to a characteristic wave period (e.g. Deike et al., 2016; Derakhti et al., 2018), there is evidence that τ_b/T_b is not fixed but instead varies with how dissipative an individual breaking event is (Perlin et al., 2013; Cao et al., 2026b). On this basis, our explicit inclusion of τ_b/T_b in (23) echos these observations and enables variations in breaking duration to be incorporated into a \mathcal{S} -based description of $\Delta E_{br}/E_0$.

4.4 The breaking strength parameter b

In this final results section, we examine how the breaking strength parameter varies across different underlying wave scales and co-flowing wind conditions. Following Tian et al. (2010); Allis (2013); Derakhti and Kirby (2016); Derakhti et al. (2018) and Craciunescu and Christou (2020), we evaluate (1) by taking $c \sim c_b$, where $c_b = 2\pi/(T_b k_b)$ is the local phase speed determined from the zero-crossing wavelength λ_b . To distinguish this particular estimate from the more general definition of b in (1), we denote it hereafter as b_b . We then consider simple parametric forms of the type $b_b \propto \mathcal{S}^\Xi$ (see (2)) and compare the resulting fits across datasets.

Figure 12 presents the behaviour of b_b in relation to different measures of wave steepness. The results in figures 12(a) and (b) show that, at a broad level, b_b for unforced (*SIREN*) breaking waves can be described by previously proposed scaling relationships. These include the $\Xi = 5/2$ power law $b_b \propto \mathcal{S}_n^{5/2}$ based on the inertial scaling of turbulent dissipation (Drazen et al., 2008; Romero et al., 2012) (figure 12a), and the approximately linear dependence on spectrally weighted steepness, $b_b \sim \mathcal{S}_s$, reported in earlier studies (Tian et al., 2010; Derakhti and Kirby, 2016; Cao et al., 2023) (figure 12b).

Note that in the latter case we relax the strict linear constraint and instead fit the present dataset using the more general threshold-type power-law form adopted in the original Cao et al. (2023) study (green line in figure 12b, coefficients listed in table 1). Although this fit is not strictly linear, it shows reasonable agreement with the literature results of T10, DK16 and C23 (figure 12b), and remains nearly linear over most of the observed range, particularly for $\mathcal{S}_s(x_I) \gtrsim 0.35$, as illustrated by the dashed linear reference line in figure 12(c). However, this parameterisation does not adequately reconcile the influence of wind forcing, as evidenced by the systematically lower values of b_b observed under stronger wind conditions (figure 12c). Such dependence is consistent with the results discussed earlier, where wind forcing was shown to promote earlier breaking and to limit both the energy dissipation rate and, consequently, b_b .

Whilst the spectrally based steepness scalings discussed above are useful for characterising the overall trends and magnitude of b_b , implementing them for field observations of individual breaking waves or whitecaps is not straightforward (De Vita et al., 2018; Cao et al., 2026a). We also acknowledge recent promising attempts to link b_b to dynamic (energetic) properties of breaking waves (Derakhti et al., 2018; Boettger et al., 2024), although these quantities are likewise non-trivial to constrain for individual events in the field. These constraints motivate us to examine local, geometry-based steepness measures that can be determined more directly from optical remote-sensing observations (Callaghan et al., 2024; Peach et al., 2025).

In this light, we examine b_b in relation to local steepness measures in figures 12(d)–(f). Although both Tian et al. (2010) and Derakhti and Kirby (2016) reported linear relationships between b_b and \mathcal{S}_b , their respective trends differ substantially and do not align well with the trend observed in the present dataset, which itself exhibits considerable scatter (figure 12d).

When $\mathcal{S}_{\text{front}}(t_b)$ is used, as shown in figures 12(e) and (f), we obtain much improved data collapse. This is observed both across unforced cases at different wave scales (relative to figure 12d)

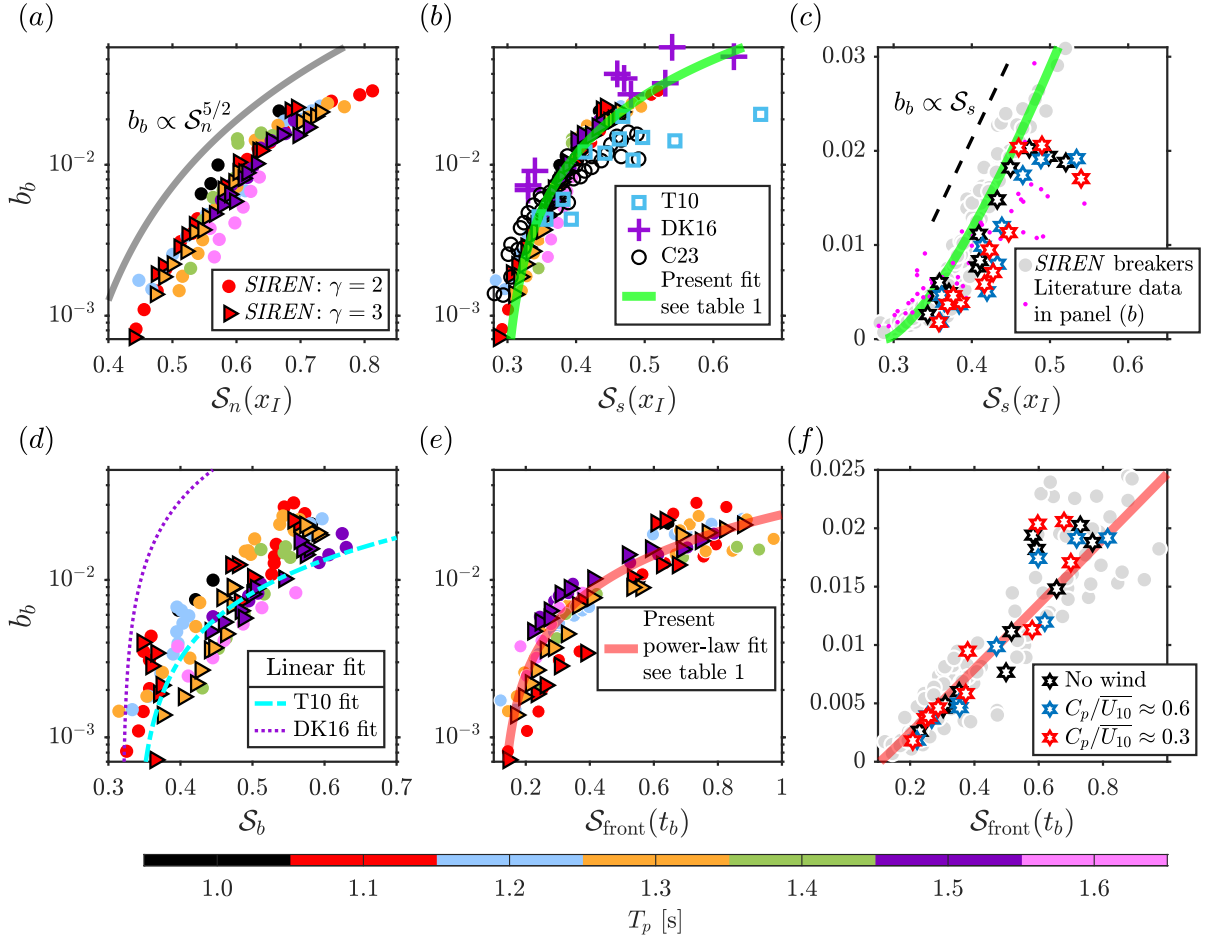


Figure 12. Relationships between the breaking strength parameter b_b calculated using equation (1), and different measures of (a–c) wave group steepness and (d–f) local steepness. The grey line in (a) shows the $\mathcal{S}_n^{5/2}$ scaling. Results derived from T10, DK16 and C23 are shown as different markers in (b), together with the linear best fit applied to the present dataset (green line). Panel (c) replots the same linear fit and includes the data from (b) in the background, shown as red dots. In (d) the purple dotted and cyan solid lines show the linear b_b – \mathcal{S}_b relationships reported respectively in DK16 and T10. The red curves in (e, f) show the power-law based parametric fit to the breaking waves in the present study. Fit coefficients for the relationships shown above are summarised in table 1.

Source	Fit coefficients			Goodness of fit
Linear fit: $b_b = \alpha_1 (\mathcal{S} - \alpha_2)$				
	α_1	α_2		r^2
Figure 12(d): T10 (Tian et al., 2010)	0.051	0.017		—
Figure 12(d): DK16 (Derakhti and Kirby, 2016)	0.40	0.32		—
Power-law fit: $b_b = \alpha_3 (\mathcal{S} - \alpha_4)^\Xi$				
	α_3	α_4	Ξ	r^2
Figures 12(b, c): green line	0.260 (± 0.094)	0.289 (± 0.024)	1.41 (± 0.30)	0.93
Figures 12(e, f): red line (24)	0.027 (± 0.002)	0.106 (± 0.088)	1.02 (± 0.29)	0.90

Table 1. Coefficients of the different parametric fits shown in figure 12. Values in parentheses denote 95% confidence intervals, and the corresponding goodness-of-fit measure is r^2 .

and under wind forced conditions (relative to figure 12c). Without imposing additional physical constraints, we constrain our data empirically using again a power-law form with a freely-tuned Ξ , yielding

$$b_b = 0.027(\mathcal{S}_{\text{front}}(t_b) - 0.106)^{1.02}, \quad (24)$$

where 0.106 is the fitted breaking onset threshold $\mathcal{S}_{\text{front}}(t_b)|_{\text{onset}}$ (see also table 1 for further details of (24) including the 95% intervals of the coefficients). The near-unity exponent in (24) implies an approximately linear dependence between b_b and the threshold-corrected crest-front steepness, although the broader generality of this empirical relation remains to be tested.

5 Conclusions

In this study, we have used laboratory measurements of unsteady, unidirectional surface wave groups to investigate breaking-induced energy dissipation and dissipation rates in individual breaking events, across a range of underlying wave scales and under both wind-unforced and co-flowing wind conditions.

Our first contribution is the development of a refined framework for quantifying the breaking-induced energy loss ΔE_{br} in physical wave flumes. Compared with the approaches commonly employed in literature, our framework more reliably accounts for background dissipation arising from wave group propagation, without introducing substantial additional measurement complexity. We learn that treatments commonly used in the past where background dissipation is not explicitly separated from ΔE_{br} can lead to a systematic overestimation of ΔE_{br} , by up to $\mathcal{O}(0.1)$ in terms of $\Delta E_{br}/E_0$ for the conditions considered here.

Using this framework, and by examining a range of steepness \mathcal{S} measures, we find that the primary influence of wave scale on both fractional energy dissipation $\Delta E_{br}/E_0$ and dissipation rate ϵ_b is through its role in setting the breaking onset. On the other hand, both $\Delta E_{br}/E(x_I)$ and ϵ_b are found to decrease systematically in the presence of co-flowing wind. This reduction is unlikely to arise from a single mechanism, but rather from a combination of wind-related effects (e.g. modifications to wave dispersion, changes in the high-frequency spectral energy content, and alterations to particle kinematics within the crest region). It is nonetheless consistent with

existing evidence that wind promotes earlier breaking and reduces the forward leaning of the crest at incipient breaking (Boettger et al., 2024; Cao et al., 2026a).

Given its demonstrated capability among the steepness measures considered to characterise both the breaking onset and the local crest geometry at incipient breaking, the crest-front steepness $\mathcal{S}_{\text{front}}(t_b)$ provides a natural basis for examining breaking energetics. Building on this, we find that, once appropriately scaled, the energy dissipation rate ϵ_b can be effectively constrained by $\mathcal{S}_{\text{front}}(t_b)$ across all breaking conditions studied here. This then leads to a scaling for fractional energy dissipation of the form $\Delta E_{br}/E(x_I) \propto \beta^* \mathcal{S}_b(\tau_b/T_b)$, where β^* is a crest-leaning parameter, \mathcal{S}_b is the local zero-crossing steepness at incipient breaking, and τ_b/T_b is the non-dimensional breaking duration. This scaling highlights that $\Delta E_{br}/E(x_I)$ depends not only on local non-linearity, but also on crest asymmetry and the breaking duration relative to the wave period. Whilst by many studies τ_b/T_b has been implicitly assumed to be fixed, our results reinforce that it plays an active role in controlling dissipation in individual breaking waves.

Finally, we revisited the breaking strength parameter $b \sim b_b$. We first confirm that the scaling laws proposed previously, including $b_b \propto \mathcal{S}_n^{5/2}$ (Drazen et al., 2008; Romero et al., 2012) and $b_b \propto \mathcal{S}_s$ (Tian et al., 2010; Derakhti and Kirby, 2016; Cao et al., 2023), capture the overall trends across much of the dataset. Motivated by practical limitations associated with applying such measures to individual breaking events in the field, we further relate b_b to locally-measured $\mathcal{S}_{\text{front}}(t_b)$. We find an approximately linear relationship between b_b and $\mathcal{S}_{\text{front}}(t_b)$, after explicitly accounting for the breaking onset threshold. Looking ahead, a natural next step involves examining how the relationships identified in this study extend to oceanic breaking waves where additional physical processes, such as the inherently three-dimensional effects, can come to play a part.

Funding

The present work is supported by the Qingdao Postdoctoral Science Foundation (Grant No. QDBSH20250202010) and the China Postdoctoral Science Foundation under grant number 2025M770858 awarded to R.C. The experimental data used here were collected during R.C.'s PhD at Imperial College London during which he was supported by the Skempton PhD Scholarship, and the experimental campaigns were funded by a NERC Standard Grant (grant number: NE/T000309/1) awarded to A.H.C.

Declaration of interests

The authors report no conflict of interest.

A Method comparisons

In this appendix we compare estimates of breaking-induced energy dissipation, ΔE_{br} , obtained using the methods of D08, T10, and C23, with those produced by the refined framework we propose in §3.3. For demonstration purposes results are presented for wave groups from the *SIREN* dataset with $\gamma = 2$ and $T_p = [1.1, 1.3, 1.5]$ s, with ΔE_{br} plotted as a function of $E(x_I)$ in figures 13(a)–(c).

We see that across all breaking conditions examined, the D08 method tends to systematically overestimate ΔE_{br} relative to the present refined framework, whilst the C23 method underestimates it. The magnitude of this overestimation (underestimation) generally increases with increasing $E(x_I)$. Estimates obtained using the T10 method and the refined framework

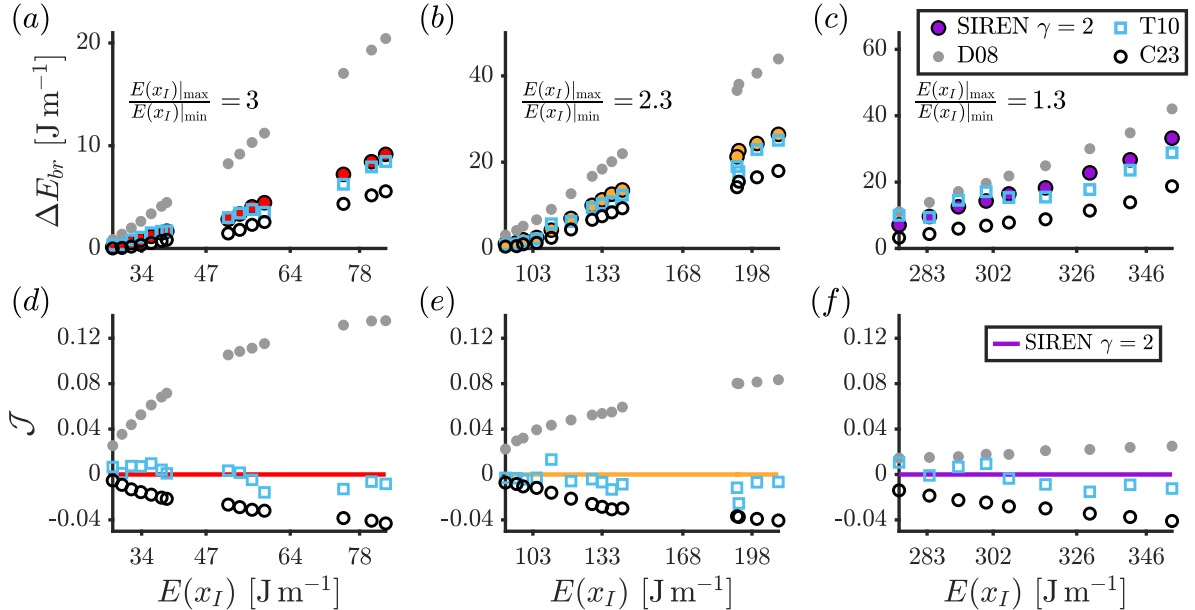


Figure 13. Comparison of calculated values of (a)–(c) breaking-induced energy dissipation ΔE_{br} and (d)–(f) \mathcal{J} based upon different methods outlined in §3 for a selection of *SIREN* breaking waves with $\gamma = 2$ and $T_p = 1.1$ s (left panels), 1.3 s (middle panels) and 1.5 s (right panels). The values of $E(x_I)|_{\max}/E(x_I)|_{\min}$ displayed in (a)–(c) indicate the ratio of the maximum to the minimum $E(x_I)$ for a given (T_p, γ) combination, highlighting how much the wave group energy has increased.

are, by contrast, similar and typically fall between the values given by D08 and C23. We also see a reduced difference in ΔE_{br} among the different methods at larger T_p (e.g. figure 13c), and this may be associated with the more limited upper bound of $E(x_I)$ that can be achieved by larger-scale wave groups (see the decreasing ratio $E(x_I)|_{\max}/E(x_I)|_{\min}$ texted from figure 13a to figure 13c).

In more quantitatively comparing different methods we define the dimensionless metric:

$$\mathcal{J} = \frac{\Delta E_{br} - \Delta E_{br, \text{calculated using the refined framework}}}{E(x_I)}, \quad (25)$$

which measures the relative deviations in breaking-induced fractional energy dissipation from the value obtained using the refined framework proposed in the present study.

The resulting values of Γ for different breaking conditions are presented in figures 13(d)–(f). Using this metric we find that the maximum overestimation (underestimation) associated with the D08 (C23) method at smaller T_p can reach approximately ~ 0.12 (~ 0.04), which reduces significantly when either $E(x_I)$ decreases or T_p increases. Consistent with the trends observed in figures 13(a)–(c), using the T10 method yields values of ΔE_{br} that are in close agreement with those obtained using the refined framework, with deviations typically within $\pm \sim 0.02$.

B Sensitivity test on the refined framework

Within the application scope our refined framework for estimating breaking-induced energy dissipation the selection of the two horizontal locations x_{b1} and x_{b2} (see figure 5b), inevitably involves a degree of subjectivity. It is therefore important to assess how sensitive the estimated ΔE_{br} is to this choice. In this appendix, we examine this sensitivity by recalculating ΔE_{br} under deliberately imposed, large variations in the horizontal breaking distance $|x_{b1} - x_{b2}|$.

Figure 14 compares the resulting fractional energy dissipation computed using halved, orig-

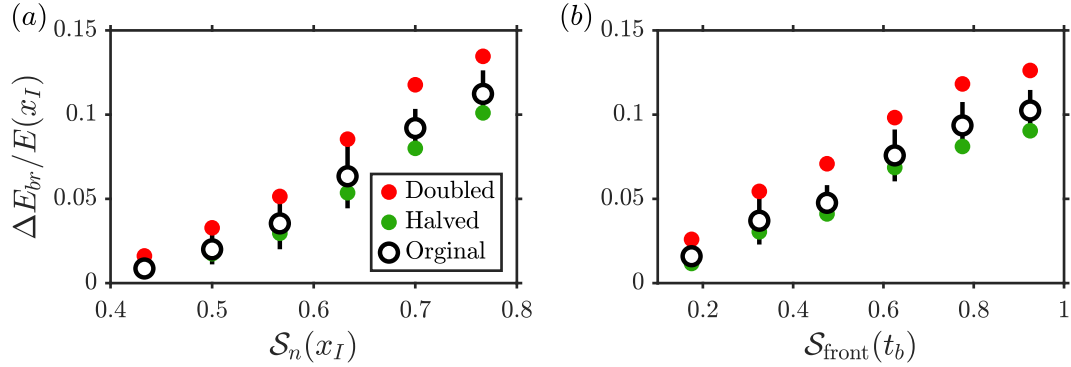


Figure 14. Bin-averaged values of the breaking-induced fractional energy dissipation plotted against (a) wave group steepness $S_n(x_I)$ and (b) crest-front steepness at incipient breaking $S_{front}(t_b)$ for bulk *SIREN* breaking wave groups, calculated using the original, halved, and doubled breaking distances $|x_{b1} - x_{b2}|$. Vertical lines indicate ± 1 standard deviation intervals of the bin averages computed using the original $|x_{b1} - x_{b2}|$.

inal, and doubled values of $|x_{b1} - x_{b2}|$, plotted against two representative measures of wave (group) steepness. The data are presented in bin-averaged form to more clearly reveal the underlying trends. As energy dissipation increases with steepness the reduction of $|x_{b1} - x_{b2}|$ by half (green dots) leads to a slight underestimation of $\Delta E_{br}/E(x_I)$, although the resulting values remain well within the standard deviation bounds associated with the original breaking distance. Conversely, even when $|x_{b1} - x_{b2}|$ is doubled (red dots), the resulting increase in $\Delta E_{br}/E(x_I)$ reaches at most ~ 0.03 at the highest steepness values considered.

Such large deviations in the effective breaking distance are, however, unlikely to arise in practice. The above results therefore indicate that the refined framework retains a high degree of robustness, with moderate subjectivity in the selection of x_{b1} and x_{b2} exerting only a limited influence on the estimated breaking-induced energy dissipation.

References

- Allis, M. J. (2013). *The Speed, Breaking Onset and Energy Dissipation of 3D Deep-Water Waves*. PhD thesis, U. New South Wales.
- Banner, M. L. and Peirson, W. L. (2007). Wave breaking onset and strength for two-dimensional deep-water wave groups. *Journal of Fluid Mechanics*, 585:93–115.
- Boettger, D. G., Keating, S. R., Banner, M. L., Morison, R. P., and Barthélémy, X. (2024). Energetic inception of breaking in surface gravity waves under wind forcing. *Physical Review Fluids*, 9:054803.
- Callaghan, A. H. (2018). On the relationship between the energy dissipation rate of surface-breaking waves and oceanic whitecap coverage. *Journal of Physical Oceanography*, 48(11):2609–2626.
- Callaghan, A. H. (2025). Estimates of the breaking strength parameter for individual oceanic whitecaps. *Geophysical Research Letters*, 52:e2025GL116342.
- Callaghan, A. H., Bidlot, J., de Leeuw, G., and O’Dowd, C. D. (2025). Comparing estimates of whitecap coverage from a spectral wave model with oceanic observations. *Geophysical Research Letters*, 52:e2024GL112996.

- Callaghan, A. H., Deane, G. B., and Stokes, M. D. (2013). Two regimes of laboratory whitecap foam decay: Bubble-plume controlled and surfactant stabilized. *Journal of Physical Oceanography*, 43(6):1114–1126.
- Callaghan, A. H., Deane, G. B., and Stokes, M. D. (2016). Laboratory air-entraining breaking waves: Imaging visible foam signatures to estimate energy dissipation. *Geophysical Research Letters*, 43(21):11320–11328.
- Callaghan, A. H., Deane, G. B., and Stokes, M. D. (2024). A comparison of laboratory and field measurements of whitecap foam evolution from breaking waves. *Journal of Geophysical Research: Oceans*, 129:e2023JC020193.
- Cao, R., Padilla, E., and Callaghan, A. (2023). The influence of bandwidth on the energetics of intermediate to deep water laboratory breaking waves. *Journal of Fluid Mechanics*, 971:A11.
- Cao, R., Padilla, E. M., Chen, X., and Callaghan, A. H. (2026a). On the limiting geometry of unsteady breaking waves subject to co-flowing wind: spectrally-informed versus locally-measured steepness. arXiv:2605.28907.
- Cao, R., Padilla, E. M., Chen, X., and Callaghan, A. H. (2026b). A representative underlying scale for spectrally resolved energy dissipation in surface breaking waves. *Journal of Geophysical Research: Oceans*, 131:e2025JC023904.
- Cao, R., Padilla, E. M., Fang, Y., and Callaghan, A. H. (2025). Identification of the free surface for unidirectional nonbreaking water waves from side-view digital images. *IEEE Journal of Oceanic Engineering*, 50:204–212.
- Craciunescu, C. C. and Christou, M. (2020). Wave breaking energy dissipation in long-crested focused wave groups based on jonswap spectra. *Applied Ocean Research*, 99:102144.
- De Vita, F., Verzicco, R., and Iafrati, A. (2018). Breaking of modulated wave groups: kinematics and energy dissipation processes. *Journal of Fluid Mechanics*, 855:267–298.
- Deane, G. B. and Stokes, M. D. (2002). Scale dependence of bubble creation mechanisms in breaking waves. *Nature*, 418:839–844.
- Deane, G. B., Stokes, M. D., and Callaghan, A. H. (2016). The saturation of fluid turbulence in breaking laboratory waves and implications for whitecaps. *Journal of Physical Oceanography*, 46:975–992.
- Deike, L. (2022). Mass transfer at the ocean–atmosphere interface: The role of wave breaking, droplets, and bubbles. *Annual Review of Fluid Mechanics*, 54:191–224.
- Deike, L., Melville, W. K., and Popinet, S. (2016). Air entrainment and bubble statistics in breaking waves. *Journal of Fluid Mechanics*, 801:91–129.
- Deike, L., Popinet, S., and Melville, W. K. (2015). Capillary effects on wave breaking. *Journal of Fluid Mechanics*, 769:541–569.
- Derakhti, M., Banner, M. L., and Kirby, J. T. (2018). Predicting the breaking strength of gravity water waves in deep and intermediate depth. *Journal of Fluid Mechanics*, 848:R2.
- Derakhti, M. and Kirby, J. T. (2014). Bubble entrainment and liquid-bubble interaction under unsteady breaking waves. *Journal of Fluid Mechanics*, 761:464–506.

- Derakhti, M. and Kirby, J. T. (2016). Breaking-onset, energy and momentum flux in unsteady focused wave packets. *Journal of Fluid Mechanics*, 790:553–581.
- Drazen, D. A., Melville, W. K., and Lenain, L. (2008). Inertial scaling of dissipation in unsteady breaking waves. *Journal of Fluid Mechanics*, 611:307–332.
- Duncan, J. (1981). An experimental investigation of breaking waves produced by a towed hydrofoil. *Proceedings of the Royal Society of London. A. Mathematical and Physical Sciences*, 377(1770):331–348.
- Galchenko, A., Babanin, A. V., Chalikov, D., Young, I. R., and Haus, B. K. (2012). Influence of wind forcing on modulation and breaking of one-dimensional deep-water wave groups. *Journal of Physical Oceanography*, 42(6):928–939.
- Gao, Q., Shen, L., and Deane, G. B. (2021). A numerical simulation framework for bubbly flow and sound generation in laboratory-scale breaking waves. *JASA Express Letters*, 1.
- Grare, L., Peirson, W. L., Branger, H., Walker, J. W., Giovanangeli, J.-P., and Makin, V. (2013). Growth and dissipation of wind-forced, deep-water waves. *Journal of Fluid Mechanics*, 722:5–50.
- Hasselmann, K. (1961). On the non-linear energy transfer on a gravity-wave spectrum. part 1. general theory. *Journal of Fluid Mechanics*, 12(4):481–500.
- Herman, A., Dragan-Górska, A., and Markuszewski, P. (2026). Close relationship between whitecapping-related wave energy dissipation and ambient sound in the open ocean. *Geophysical Research Letters*, 53:e2025GL120342.
- Hogan, L., Zappa, C. J., Cifuentes-Lorenzen, A., Edson, J. B., O’Donnell, J., and Ullman, D. S. (2025). Observations of breaking wave dissipation and their relationship to atmosphere-ocean energy transfer. *Journal of Geophysical Research: Oceans*, 130:e2024JC022130.
- Iafrazi, A. (2011). Energy dissipation mechanisms in wave breaking processes: Spilling and highly aerated plunging breaking events. *Journal of Geophysical Research: Oceans*, 116(7):1–22.
- Iafrazi, A., Vita, F. D., and Verzicco, R. (2019). Effects of the wind on the breaking of modulated wave trains. *European Journal of Mechanics - B/Fluids*, 73:6–23.
- Knobler, S., Winiarska, E., Babanin, A., and Liberzon, D. (2022). Wave breaking probabilities under wind forcing in open sea and laboratory. *Physics of Fluids*, 34:032122.
- Kway, J. H. L., Loh, Y. S., and Chan, E. S. (1998). Laboratory study of deep-water breaking waves. *Ocean Engineering*, 25(8):657–676.
- Liu, C., Hu, Y., Yang, X., and Hu, C. (2024). Numerical study of bubble rise in plunging breaking waves. *Physics of Fluids*, 36.
- Liu, S., Wang, H., Bayeul-Lainé, A.-C., Li, C., Katz, J., and Coutier-Delgosha, O. (2023). Wave statistics and energy dissipation of shallow-water breaking waves in a tank with a level bottom. *Journal of Fluid Mechanics*, 975:A25.
- McAllister, M., Pizzo, N., Draycott, S., and van den Bremer, T. (2023). The influence of spectral bandwidth and shape on deep-water wave breaking onset. *Journal of Fluid Mechanics*, 974:A14.

- McAllister, M. L., Draycott, S., Calvert, R., Davey, T., Dias, F., and van den Bremer, T. S. (2024). Three-dimensional wave breaking. *Nature*, 633:601–607.
- Melville, W. K. (2003). The role of surface-wave breaking in air-sea interaction. *Annual Review of Fluid Mechanics*, 28(28):279–321.
- Mostert, W., Popinet, S., and Deike, L. (2022). High-resolution direct simulation of deep water breaking waves: transition to turbulence, bubbles and droplets production. *Journal of Fluid Mechanics*, 942:A27.
- Padilla, E. M., Cao, R., and Callaghan, A. H. (2023). Spatial interpolation of wave fields based on limited spatial measurements. *IEEE Journal of Oceanic Engineering*, 48:1226–1235.
- Peach, J., Callaghan, A. H., Bergamasco, F., Pistellato, M., Barbariol, F., and Benetazzo, A. (2025). A vision-based method for spatial and temporal tracking of individual whitecaps from breaking ocean waves. *IEEE Transactions on Geoscience and Remote Sensing*, 63:1–15.
- Perlin, M., Choi, W., and Tian, Z. (2013). Breaking waves in deep and intermediate waters. *Annual Review of Fluid Mechanics*, 45(1):115–145.
- Perlin, M. and Schultz, W. W. (2000). Capillary effects on surface waves. *Annual Review of Fluid Mechanics*, 32(1):241–274.
- Qi, Y., Xu, X., Tan, S., Zhong, S., Wu, Q., and Ni, R. (2024). Breaking bubbles across multiple time scales in turbulence. *Journal of Fluid Mechanics*, 983:A24.
- Ramberg, S. E. and Griffin, O. M. (1987). Laboratory study of steep and breaking deep water waves. *Journal of Waterway Port Coastal and Ocean Engineering*, 113(5):493–506.
- Rapp, R. J., Melville, W. K., and Longuet-Higgins, M. S. (1990). Laboratory measurements of deep-water breaking waves. *Philosophical Transactions of the Royal Society of London. Series A, Mathematical and Physical Sciences*, 331(1622):735–800.
- Romero, L., Melville, W. K., and Kleiss, J. M. (2012). Spectral energy dissipation due to surface wave breaking. *Journal of Physical Oceanography*, 42:1421–1444.
- Saket, A., Peirson, W. L., Banner, M. L., Barthelemy, X., and Allis, M. J. (2017). On the threshold for wave breaking of two-dimensional deep water wave groups in the absence and presence of wind. *Journal of Fluid Mechanics*, 811:642–658.
- Saulnier, J.-B., Clément, A., de O. Falcão, A. F., Pontes, T., Prevosto, M., and Ricci, P. (2011). Wave groupiness and spectral bandwidth as relevant parameters for the performance assessment of wave energy converters. *Ocean Engineering*, 38:130–147.
- Scapin, N., Wu, J., Farrar, J. T., Chapron, B., Popinet, S., and Deike, L. (2026). Growth rate and energy dissipation in wind-forced breaking waves. *Geophysical Research Letters*, 53:e2025GL117901.
- Sinnis, J. T., Grare, L., Lenain, L., and Pizzo, N. (2021). Laboratory studies of the role of bandwidth in surface transport and energy dissipation of deep-water breaking waves. *Journal of Fluid Mechanics*, 927:A5.
- Tian, Z., Perlin, M., and Choi, W. (2008). Evaluation of a deep-water wave breaking criterion. *Physics of Fluids*, 20:066604.

- Tian, Z., Perlin, M., and Choi, W. (2010). Energy dissipation in two-dimensional unsteady plunging breakers and an eddy viscosity model. *Journal of Fluid Mechanics*, 655:217–257.
- Tian, Z., Perlin, M., and Choi, W. (2012). An eddy viscosity model for two-dimensional breaking waves and its validation with laboratory experiments. *Physics of Fluids*, 24(3):036601.
- Touboul, J. and Banner, M. L. (2021). On the breaking inception of unsteady water wave packets evolving in the presence of constant vorticity. *Journal of Fluid Mechanics*, 915:A16.
- Wu, C. H. and Nepf, H. M. (2002). Breaking criteria and energy losses for three-dimensional wave breaking. *Journal of Geophysical Research*, 107(C10):3177.
- Wu, C. H. and Yao, A. (2004). Laboratory measurements of limiting freak waves on currents. *Journal of Geophysical Research*, 109(C12):C12002.
- Xu, H., Chen, Y., Cao, R., Tang, T., Du, M., Li, J., Callaghan, A. H., and Zhang, D. (2025). Generative discovery of partial differential equations by learning from math handbooks. *Nature Communications*, 16:10255.
- Xu, Y., Liang, S., Sun, Z., and Xue, Q. (2022). A new spectral parameter to predict dominant wave breaking based on the jonswap spectrum. *Ocean Engineering*, 243:110332.
- Zhang, S. (2005). Energy and momentum dissipation through wave breaking. *Journal of Geophysical Research*, 110(C9):1–13.
- Zhang, Y., Liang, S., and Sun, Z. (2019). Study on energy spectrum instability in the processes of propagating and breaking of focusing waves. *China Ocean Engineering*, 33(1):86–93.
- Zou, X., Babanin, A. V., Schulz, E. W., Manasseh, R., and Guan, C. (2022). Passive acoustic determination of spectral wave breaking dissipation. *Journal of Physical Oceanography*, 52:2807–2823.